Turbulence structures of supersonic boundary layers in a bent pipe

Huifeng Chen (陈慧锋), Yixin Yang (杨揖心),* Mingbo Sun (孙明波),†
Hongbo Wang (汪洪波), Dapeng Xiong (熊大鹏), Changhai Liang (梁昌海),
Wenxiao Long (龙文骁), and Wenming Li (李文明)
National University of Defense Technology, Changsha, Hunan 410073, China

(Received 8 March 2026; accepted 11 August 2026; published 27 August 2026)

Direct numerical simulation is performed to investigate supersonic flows in a bent pipe with a developing turbulent boundary layer and a core-flow region. By comparison with a flat plate, a channel, and a straight pipe, instantaneous and time-averaged flow fields in the bent pipe indicate intricate flow phenomena, including waves, separation, secondary flows, and the Görtler instability. Expansion and compression waves are generated on the upper (convex) and lower (concave) sides, respectively. Separation is triggered by the combined effects of the adverse pressure gradient (APG) and flow deceleration on the upper wall, which significantly thickens the boundary layer and enhances the velocity fluctuations. Driven by the imbalance of the centrifugal force and pressure gradients, secondary flows (Dean vortices) are visualized in the circumferential boundary layer. On the lower wall, the quantitative evidence of the Görtler number distribution, the clustering and uplift of low-momentum fluids, and the presence of streamwise counterrotating vortices with large-scale wavelengths are related to the increase of the Görtler instability. The baroclinic effect induced by Görtler-type vortices promotes the formation of small-scale vortices and intensifies the Reynolds stresses and turbulent kinetic energy in the outer region of the boundary layer. The occurrence of favorable pressure gradient stabilizes the lower boundary layer and causes the turbulence decay. Quadrant decomposition analysis reveals that the increasing Görtler instability and APG can amplify ejections (Q2) and sweeps (Q4) of turbulence events, while the FPG will suppress sweeps (Q4).

DOI: 10.1103/kv7h-484s

I. INTRODUCTION

Supersonic boundary layers have been a significant research area for decades, owing to their critical role in predicting the aerodynamic performance of high-speed flight vehicles. Although the studies on turbulent boundary layers are typically conducted on flat plates [1–5] or in channels [6–10], boundary layers within bent pipes (or curved pipes) are of considerable practical interest in various aerospace applications. For instance, boundary-layer flows can significantly affect the performance of aircraft intakes, nozzles, fuel injectors, and serpentine diffusers. Pipe flows have been extensively studied, with a predominant focus on compressible and incompressible flows in straight pipes [11–16]. However, most studies on flows in bent pipes have focused on incompressible flows [17–22], while compressible scenarios have received less attention. Since bent pipes have an important effect in the manufacturing of high-speed vehicles, elucidating the physical processes that drive supersonic boundary-layer flows in bent pipes is crucial for advancing the design of more efficient air-breathing aircrafts.

*Contact author: yangyixin@nudt.edu.cn
†Contact author: sunmingbo@nudt.edu.cn

Bent pipes play an essential role in nearly all industrial processes, including power production, manufacturing, refrigeration, and space applications [23]. Recent experimental and computational advances in bent-pipe flows were summarized by Vester *et al.* [24], and the characteristics of secondary flows were documented by Stanitz *et al.* [25]. In this study, secondary flow is regarded as a phenomenon in which the fluid motion is aligned with the vorticity component parallel to the main flow direction, characterized by the rotational properties of the flows. In gradual bends, secondary flow develops with a pair of streamwise counterrotating vortices, called Dean vortices [26]. Under incompressible conditions, these are considered helical or Dean flows, which have been extensively investigated in curved channels, rectangular ducts, and circular pipes [27–30]. Under supersonic conditions, the asymmetry of turbulent boundary layers in a bent pipe originates fundamentally from secondary flows driven by the centrifugal force and pressure gradients and the interaction between the oblique shock and shear layer, thereby promoting the vortex generation and turning the boundary-layer flows [31]. The presence of secondary flows within the boundary layers also promote circumferential transport of mass and energy from the concave to the inner convex side through the lateral wall [32,33]. Furthermore, the unsteady undulation or periodic oscillation of Dean vortices leads to changes in the turbulent structures of boundary layers, including the orientation of velocity streaks and stagnation point movement, are considered generation mechanisms for very-large-scale motion (VLSM) in bent pipes [20–22].

The development of turbulent boundary layers in bent pipes, which commonly arises in industrial applications, has not been thoroughly investigated [19], but experimental and numerical investigations of boundary layers on curved surfaces have been conducted for a long time. When the supersonic flow enters a bend, the concave and convex sides of the developing boundary layers are affected differently by the pipe wall curvature. Compared with the turbulence structures of the flat-plate boundary layer with zero pressure gradients (ZPGs), those on the curved surface are not only associated with the curvature parameter, but also affected by local pressure gradients and the interaction with waves. Prior studies [34–36] have indicated that the convex surface curvature has a negative contribution to the near-wall Reynolds stresses and turbulent kinetic energy, thereby stabilizing the boundary layer. As supersonic flows pass over a convex wall, the boundary layers are strongly affected by the bulk dilatation of extra strain rates, in addition to the shear velocity gradient [37]. The boundary-layer flow is then accelerated by an expansion fan, leading to a decrease in the density and pressure. Consequently, the expansion process is typically associated with streamwise favorable pressure gradients (FPGs), which can lead to turbulence decay but promote the stabilization of the boundary layer [38,39]. Mokhtarzadeh-Dehghan and Yuan [40] measured turbulence quantities of the developing turbulent boundary layers in a 90° square bend and reported that the reduction in turbulence on the convex wall was particularly pronounced in the outer 80% of boundary layers. Further, the response of the wall-normal intensity to the removal of curvature was slower than that of the streamwise intensity. Moreover, Muck *et al.* [35] reported that the boundary layer subjected to convex curvature attenuated existing turbulent structures without producing new types of vortices, whereas the response of the boundary layer to concave curvature involved the reorganization of vortical structures.

In contrast to the convex wall, the turbulence enhancement on the concave wall is pronounced in the boundary layers. The concave curvature leads to substantial distortion in compressible boundary-layer flows owing to various intertwined influences, such as bulk compression at extra strain rates, streamwise and wall-normal pressure gradients, centrifugal instability, and generation and reorganization of vortices [36,41,42]. Neel *et al.* [43] studied the impact of adverse pressure gradients (APGs) resulting from streamline curvature on the hypersonic boundary layer of Mach 4.9 and revealed a significant straightening of shear stresses within the boundary layer across the APG region, where the thinning effect of the boundary layer was attributed to an APG. Barlow and Johnston [44] posited that the concave wall curvature amplified the large-scale motions perpendicular to the wall and that the intensified influx and outflux of large scales enhance turbulence mixing within boundary layers, leading to a significant increase in the skin friction. In addition, an unstable mode of turbulence can be triggered by the imbalance between the centrifugal force and wall-normal pressure gradients, namely, the Görtler instability [45], which occurs generally under external motivations such as APGs [46] and some artificial disturbances [47,48]. This instability is characterized by a dimensionless parameter, the Görtler number, which is defined as $G_\theta = \mathrm{Re}_\theta\sqrt{\theta/R}$, where Re_θ is the Reynolds number based on the boundary-layer momentum thickness θ, and R is the curvature radius of the curved surface. Although both Görtler and Dean vortices are caused by streamwise curvature due to centrifugal instabilities and share the same physical mechanisms [49], their morphological characteristics and evolution patterns differ fundamentally [27]. Classical Görtler vortices were initially observed in the laminar incompressible flows over the concave wall, which is the focus of most existing studies on the Görtler instability [46,50–52]. Görtler-type vortices can be generated even in compression ramps [53–56], shock-wave–boundary-layer interaction [57–59] and fully developed turbulent boundary layers [37,41,60]. Studies on the coherent structures of Görtler vortices in compressible flows have also been reported, including experiments by Ciolkosz and Spina [61], Wang *et al.* [62], and Chen *et al.* [63], as well as the theoretical and numerical works by Viaro and Ricco [64] and Sun *et al.* [65]. Wang *et al.* [62] suggested that the transition from laminar boundary layers to turbulence was achieved more rapidly for compressible Görtler vortices than for incompressible counterparts. This is because the secondary instability of the nonlinear evolution can be increased in response to the Mach number [64]. Furthermore, Wang *et al.* [66] revealed that the Görtler instability within the supersonic boundary layers intensified the accumulation of new vortices and promoted large-scale streamwise roll cells to enhance the interaction between low- and high-momentum flows, thereby increasing the turbulent intensity in the outer region of boundary layers.

Given the current lack of systematic investigations into compressible boundary layers in bent pipes, this study aims to clarify the mechanisms underlying turbulent boundary layer behaviors and the coupling effects of the geometric curvature and flow compressibility. In this study, DNS is employed to gain a comprehensive understanding of the characteristics and turbulent structures of supersonic boundary layers in bent pipes. By analyzing the spatial distributions of flow variables, the impacts of pressure gradients, and corresponding changes in the Reynolds stresses and turbulent kinetic energy, this study aims to elucidate the underlying mechanism governing the development of turbulent boundary layers. Specifically, separation, the Görtler instability, secondary flows, waves, and vortices are included in the scope of this research. The remainder of this paper is organized as follows. The details of geometries, numerical methods, and relevant computational setups are introduced in Sec. II A. Numerical validation and a comparison of boundary layers on the straight configurations including a flat plate, a channel, and a pipe are implemented in Sec. II B. In Sec. III A, both instantaneous and time-averaged properties of the flow fields are analyzed to disclose complex flow phenomena within the bent pipe considered in this study. The Görtler instability within the outer boundary layer is discussed in Sec. III B, and the response of turbulence to the curvature in bent pipes is illustrated in Sec. III C. Finally, the conclusions of this study are presented in Sec. IV.

II. METHODOLOGY

A. Computational methods and setups

The supersonic flow considered herein is governed by the three-dimensional compressible Navier-Stokes (NS) equations for a perfect gas. In Cartesian coordinates, they are expressed as follows:

$$\frac{\partial \rho}{\partial t} + \frac{\partial}{\partial x_j}(\rho u_j) = 0, \tag{1}$$

$$\frac{\partial}{\partial t}(\rho u_i) + \frac{\partial}{\partial x_j}(\rho u_i u_j + p\delta_{ij}) = \frac{\partial \tau_{ij}}{\partial x_j}, \tag{2}$$

$$\frac{\partial}{\partial t}(\rho E) + \frac{\partial}{\partial x_j}[(\rho E + p)u_j] = \frac{\partial}{\partial x_j}\left(\tau_{ij}u_i + k\frac{\partial T}{\partial x_j}\right), \tag{3}$$

where t is the time variable; x_i (also as x, y, and z; $i = 1$, 2, and 3) is the ith coordinate and u_i (also as u, v, and w) is the corresponding velocity component; ρ, p, and T denote the density, the pressure, and the temperature of the fluid, respectively; $E = \int_0^T C_v dT + \frac{1}{2}u_i^2$ represents the total energy; the thermal conductivity coefficient k can be obtained from the dynamic viscosity μ and the Prandtl number $\mathrm{Pr} = 0.72$ as $k = \mu C_p/\mathrm{Pr}$; $\tau_{ij} = -\frac{2}{3}\mu\frac{\partial u_i}{\partial x_j}\delta_{ij} + \mu(\frac{\partial u_i}{\partial x_j} + \frac{\partial u_j}{\partial x_i})$ represents the shear stress tensor; and δ_{ij} refers to the Kronecker symbol.

In addition, the specific heat ratio $\gamma = C_p/C_v \approx 1.39$ is the ratio of the specific heat of constant pressure C_p to the specific heat of constant volume C_v, and the gas constant $R_g = R_u/M_g$ is the ratio of the universal gas constant $R_u \approx 8.314\,\mathrm{J/(mol\,K)}$ to the molar mass of the gas molecules M_g. NS equations become closed form by applying the state equation of the thermally perfect gas $p = \rho R_g T$. Sutherland's law is used to predict the dynamic viscosity μ of the fluid as $\frac{\mu}{\mu_{\mathrm{ref}}} = (\frac{T}{T_{\mathrm{ref}}})^{3/2}\frac{T_{\mathrm{ref}}+T_s}{T+T_s}$, where the reference dynamic viscosity takes a value of $\mu_{\mathrm{ref}} = 1.716\times10^{-5}\,\mathrm{kg\,m^{-1}\,s^{-1}}$ at the reference temperature $T_{\mathrm{ref}} = 273.15$ K, and $T_s = 110.4$ K is the Sutherland constant temperature for air. The computation simulates the free-stream inflow with a total pressure of $p_{0,\infty} = 101325$ Pa, stagnation temperature of $T_{0,\infty} = 300$ K, and Mach number of $\mathrm{Ma}_\infty = u_\infty/\sqrt{\gamma R_g T_\infty} = 3$.

The synthetic eddy method (SEM) developed by Xiong *et al.* [67] and Long *et al.* [68] is used in this study as an inflow turbulence generator. Although this method was originally proposed for large eddy simulation [69], it has also been successfully applied to direct numerical simulation (DNS) of bent pipes [22,33]. As reviewed by Wu [70], for wall-bounded anisotropic flows, SEM directly models the representative coherent eddies of turbulent flows from a structural perspective. Based on Taylor's frozen turbulence hypothesis, the turbulent flow is assumed to be dispersed by a predetermined quantity of virtual turbulent spots, each of which is characterized by a unique spatial-temporal shape function. The Gaussian distribution is adopted as the shape function to maintain the two-point correlation, which is consistent with that used by Jarrin *et al.* [69].

A hybrid EC/WENOCU4 scheme [71] is applied in the numerical simulation. The discretization of convective terms couples an energy-conservation (EC) fourth-order central difference scheme and an optimized weighted essentially nonoscillatory central-upwind fourth-order (WENOCU4) shock-capturing scheme, with the advantages of high precision and low dissipation. The underlying concept of this hybrid algorithm is that the shock-capturing WENOCU4 scheme is activated in these critical cells to ensure the stability of the calculation, whereas the EC scheme is employed for the other parts of the flow field with smooth scales to improve the accuracy of the calculation. The switch between the EC and WENOCU4 schemes is determined by the shock sensor proposed by Zhao *et al.* [72] Moreover, the time advancement is performed using the third-order explicit Runge-Kutta scheme. The NS equations are solved directly in an in-house computational solver developed by Lai *et al.* [73]. This solver has been widely applied in numerical studies of supersonic flows such as transverse jets [74], wall-bounded flows [33,75], and even combustion [76,77].

Four types of computational domains are investigated in this study: the flat-plate boundary layer (FBL), channel boundary layer (CBL), straight pipe (SP), and bent pipe (BP). The flow over a flat plate or channel is confined in the y direction but free in the z direction, shaping the boundary layer of the FBL or CBL as a plane; it is considered to be quasi-two-dimensional, and referred to as planar flows. Conversely, the wall confinements of pipe flows (the SP and BP) are in both the y and z directions, forming the cylindrical boundary layers. When comparing the planar and pipe flows, the latter exerts a more pronounced three-dimensional influence on the turbulent boundary layer than the former. At the entrance of the computational domain, the central region adopted the uniform inflow condition, and the boundary-layer region with a predetermined thickness from the wall is addressed using the SEM. The outflow is under the nonreflecting boundary condition, and the wall condition is assumed to be no slip and adiabatic.

As depicted in Fig. 1, each of computational domains consists of two parts: a developing region located upstream and a critical simulation region located downstream. For planar flows shown in Fig. 1(a), buffer regions are included to dissipate the fluctuations on two sides of the rectangular

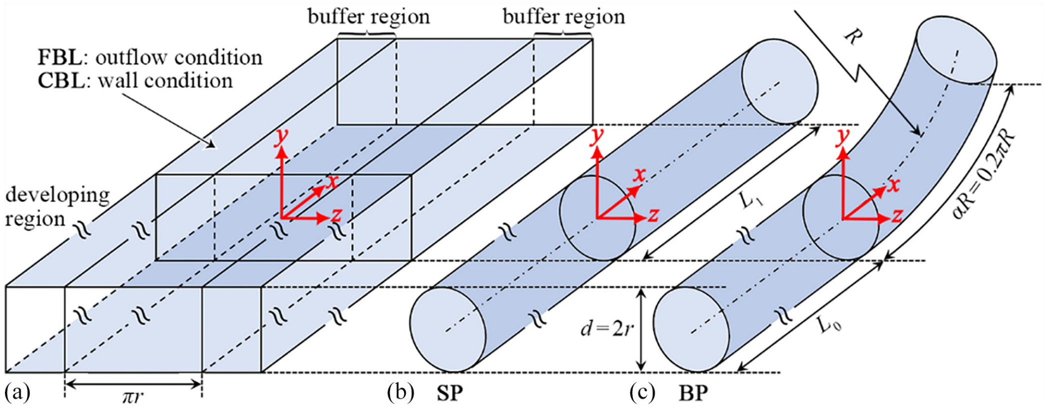

FIG. 1. Geometries of the computational domains employed in this study, including the (a) FBL and CBL, (b) SP, and (c) BP.

domain where the boundary conditions in the spanwise direction are symmetric. The characteristic height of channel ($d/2$) is consistent with the pipe radius r, and the width of the rectangular domain is set to half the circumference of the circular pipe cross section, which is πr. For pipe flows, the length of the straight developing region L_0 is the same as that of plane flows. The bend or the bent section in the BP [see Fig. 1(c)] is tangent to the upstream straight section, with a streamwise curvature radius of R and a total bending angle of $\alpha = 0.2\pi$ (in rad). Moreover, the length of the critical simulation region in the SP [see Fig. 1(b)] is consistent with the bend in the BP, which is $L_1 = \alpha R$.

The boundary-layer thickness at the inlet of all computational domains set for the SEM is $\delta_0 = 0.227r$, which increases to $\delta_i \approx 0.25r$ after the boundary layer developed over the straight section to enter the critical simulation region. The development of turbulent boundary layers is analyzed in Sec. III A. When the length is converted into a relative expression, $L_0 = 40\delta_0 \approx 9.09r$, $L_1 \approx 30\delta_i \approx 7.62r$, $R \approx 48\delta_i$, $d \approx 8\delta_i$, and $r/R = 0.0825$. Therefore, the space for the development of boundary layers in the flat plate, the channel, and circular pipes is sufficient, and the curvature of the pipe bend is much smaller compared to that in prior incompressible studies [17,18,21]. In the present calculations, the simulation was run for approximately $285\delta_i/u_\infty$, which corresponds to approximately 9.5 flow-through times, to achieve a quasisteady flow pattern. On this basis, the time-averaging process starts over a duration of $150\delta_i/u_\infty$, which is equivalent to 5 flow-through times.

The dimensionless flow parameters obtained from the end of the developing region, which is also the inlet of the critical simulation region, are listed in Table I. Hereinafter, the Reynolds numbers are defined as $\mathrm{Re}_\tau = \overline{\rho}_w u_\tau \delta_i/\overline{\mu}_w$, $\mathrm{Re}_\theta = \rho_\infty u_\infty \theta_i/\mu_\infty$, and $\mathrm{Re}_{\delta_2} = \rho_\infty u_\infty \theta_i/\overline{\mu}_w$, respectively; the Dean number is $\mathrm{De} = \mathrm{Re}_\theta\sqrt{r/R}$ in this study; δ_i and θ_i represent the 99% boundary-layer thickness and

TABLE I. Information of flow parameters for computational setups and grids of different cases in this study.

Case	Ma_∞	Re_τ	Re_θ	Re_{δ_2}	De	$\frac{\overline{\Delta x^+}}{(\Delta L^+)}$	$\frac{\Delta x^+_{\max}}{(\Delta L^+_{\max})}$	$\frac{\overline{\Delta y^+}}{(\Delta r^+)}$	$\frac{\Delta y^+_{\min}}{(\Delta r^+_{\min})}$	$\frac{\Delta y^+_{\max}}{(\Delta r^+_{\max})}$	$\frac{\overline{\Delta z^+}}{(\Delta (r\theta)^+)}$	$\frac{\Delta z^+_{\max}}{(\Delta (r\theta)^+_{\max})}$
FBL	3.0	235	3559	1453	0	6.86	6.86	1.88	0.55	5.22	7.48	7.48
CBL	3.0	235	3262	1332	0	6.86	6.86	1.88	0.55	5.22	7.48	7.48
SP	3.0	231	2743	1120	0	6.90	6.90	1.89	0.55	5.25	6.35	7.53
BP	3.0	229	2869	1171	824	6.16	7.46	1.87	0.55	5.19	6.28	7.45

the momentum thickness measured at the inlet of the critical simulation region, respectively; μ_∞ is the dynamic viscosity in the free-stream inflow and $\overline{\mu}_w$ refers to its average estimation on the wall; the friction velocity $u_\tau = \sqrt{\overline{\tau}_w/\overline{\rho}_w}$ is derived from the wall shear stress $\overline{\tau}_w$ and density $\overline{\rho}_w$; grid points are distributed in the streamwise, wall-normal, and spanwise directions in the planar flows (the FBL and CBL), i.e., the x, y, and z directions, whereas they are distributed in the streamwise, radial, and azimuthal directions in the circular pipes (the SP and BP), i.e., the L, r, and θ directions; Δ denotes the grid interval or the grid spacing; the superscript "+" indicates the length normalized by the wall viscous unit $\delta_\upsilon = \overline{\mu}_w/\sqrt{\overline{\rho}_w\overline{\tau}_w}$; and the subscript "min" or "max" represent the minimum or the maximum. Although the FBL, CBL, and SP have a consistent curvature of zero (hence referred to as straight configurations or zero-curvature cases) and are under the same inflow and wall conditions, the data show differences in the development of boundary layers; this is further discussed in this section. The friction Reynolds numbers Re_τ for the four cases are all approximately 230, with the corresponding Re_θ within $2700 \sim 3600$ and Re_{δ_2} within $1100 \sim 1500$. Furthermore, the Dean number of the bent-pipe flow is 824. In the wall-normal or the radial direction, the first off-wall grid point is located at $\Delta y_w^+ = 0.55$ and the average interval is estimated to be $\overline{\Delta y^+} \approx 1.9$, indicating that the current grids have sufficient small-scale resolution in analyzing critical flow parameters of the boundary layer. The streamwise and spanwise grid intervals for rectangular domains (Δx^+ and Δz^+) or the streamwise and azimuthal grid intervals for circular pipes (ΔL^+ and $\Delta(r\theta)^+$) are less than 8, which means that the overall quality of the grid setting can absolutely meet the high standards of DNS, and lays a strong foundation for performing well to identify the fine-scale turbulent coherent structures in all directions.

B. Numerical validation

First, zero-curvature flows (the FBL, CBL, and SP) are considered to verify the reliability of DNS data for predicting boundary-layer characteristics. This categorization enables the isolation of the effect of geometric confinements on the flow by focusing on scenarios in which streamwise curvature is absent. In this study, the CBL and SP exhibit features similar to the FBL, including a developing boundary layer attached to the wall and a core flow region farther from the wall. Therefore, this study is distinct from prior comparative study [78] on wall-bounded shear flows in pipes, channels, and flat-plate boundary layers. Extensive literature [7,79,80] agrees on the similarity in the inner regions of pipe and channel flows, but also conveys that the mean velocity profiles will be different as compared to turbulent boundary layers, especially in the outer regions.

In the subsequent analysis and discussion, the instantaneous flow-field data obtained from the computation is conducted by the Reynolds decomposition: $f = \bar{f} + f'$, where f can be any one of flow variables such as ρ, u, v, w. In this work, the mean statistics of velocity fluctuations are normalized by the friction velocity (with the superscript "+"), that is, $\langle u_i u_j\rangle^+ = \overline{u'_i u'_j}/u_\tau^2$. For the diagonal components ($i = j$), the root-mean square of velocity fluctuations (with the additional subscript "rms") can be calculated as $\langle u_i u_i\rangle^+_{\mathrm{rms}} = \sqrt{\overline{u'_i u'_i}}/u_\tau$. To take the influence of flow compressibility into consideration, the Reynolds stresses are measured by $\tau^+_{ij} = (\bar{\rho}/\bar{\rho}_w)\langle u_i u_j\rangle^+$ because Morkovin [81] indicates that compressible turbulence statistics at moderate Mach numbers (typically below 5) exhibit similarity to incompressible counterparts when scaled with local mean density. As the validity of Morkovin's hypothesis has been addressed in extensive studies [1,82,83], the van Driest transformation [84] is widely applicable to the mean velocity profile of the compressible boundary layer, as $u_{\mathrm{VD}} = \int_0^{\bar{u}} \sqrt{\bar{\rho}/\bar{\rho}_w}\mathrm{d}\bar{u}$. In the representation of velocity profiles, the van Driest transformed mean velocity is normalized by the friction velocity $u^+_{\mathrm{VD}} = u_{\mathrm{VD}}/u_\tau$, and the wall-normal distance is scaled by the wall viscous unit $y^+ = y_w/\delta_\upsilon$.

The three types of zero-curvature flows (the FBL, CBL, and SP) in this study are compared with the results of flat-plate boundary layers, channels, and pipes from prior studies, as depicted in Fig. 2. The present DNS data are obtained at the selected positions $x = 65\delta_0$ for the FBL, $x = 38\delta_0$ for the CBL, and $x = 42\delta_0$ for the SP, so as to match the friction Reynolds numbers of the reference data for quantitative comparison. To facilitate the comparison of statistics from turbulent

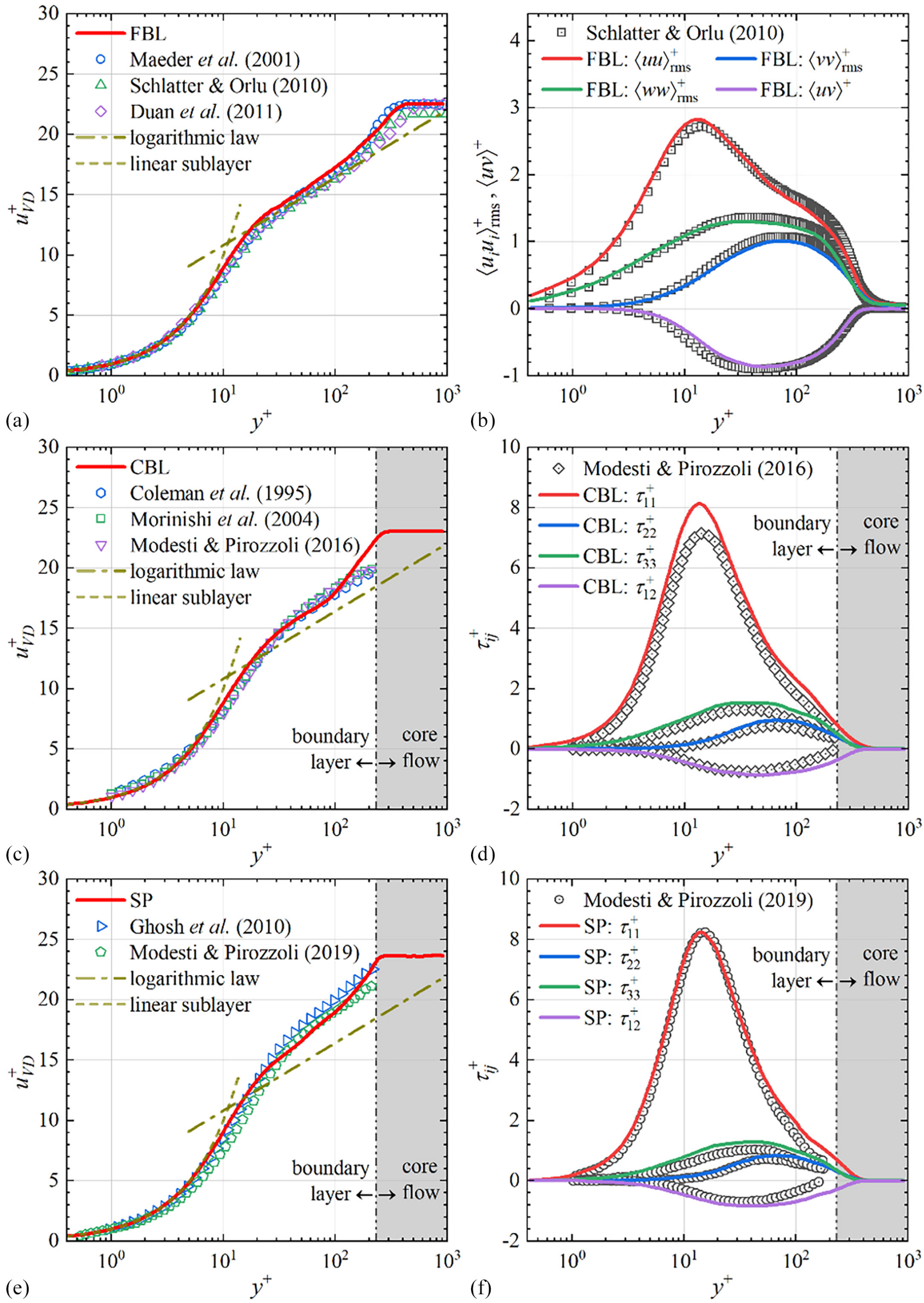

FIG. 2. Wall-normal distributions of (a), (c), (e) the van Driest transformed mean velocity and (b) velocity fluctuations or (d), (f) the Reynolds stresses in the (a), (b) FBL, (c), (d) CBL, and (e), (f) SP. The dashed line denotes the linear sublayer: $u^+ = y^+$, and the dotted-dashed line denotes the logarithmic law: $u^+ = \ln(y^+)/0.41 + 5.2$. Comparisons are made with the results of (a) Maeder *et al.* [2], (a), (b) Schlatter and Örlü [85], (a) Duan *et al.* [86], (c) Coleman *et al.* [87], (c) Morinishi *et al.* [88], (c), (d) Modesti and Pirozzoli [8], (e) Ghosh *et al.* [7], and (e), (f) Modesti and Pirozzoli [16].

flows in the CBL and SP, the regions of the boundary layer and core flow are specially labeled in Figs. 2(c)–2(f). By comparison, the FBL agrees well with the results from supersonic boundary layers of Maeder *et al.* [2] and Duan *et al.* [86] and the incompressible boundary layer of Schlatter and Örlü [85]. In addition, the curve essentially follows the linear law $u^+ = y^+$ and the logarithmic law $u^+ = \ln(y^+)/\kappa + B$, with the von Kármán constant $\kappa = 0.41$ and the additive constant $B = 5.2$. The root-mean square of velocity fluctuations $\langle u_i u_i \rangle^+_{\rm rms}$ and $\langle uv \rangle^+$ are compared with the data from Schlatter and Örlü [85], and good agreement is noted. Figures 2(a) and 2(b) confirm the prediction accuracy of the velocity and its fluctuations in the supersonic boundary layer under the current flow condition. In Fig. 2(c), the CBL exhibits good agreement with the fully developed channel flows of Coleman *et al.* [87], Morinishi *et al.* [88], and Modesti and Pirozzoli [8] within the range of $y^+ \lesssim 100$. The Reynolds stresses of the CBL in Fig. 2(d) show that in addition to minor differences in τ^+_{22}, τ^+_{33} and τ^+_{12} compared to the results of Modesti and Pirozzoli [8], the position of the peak of τ^+_{11} is accurately predicted, while its amplitude is larger than that of the reference data. The van Driest transformed mean velocity profile in SP at $\mathrm{Re}_\tau = 231$ is compared with the compressible pipe flows at similar friction Reynolds numbers from Modesti and Pirozzoli [16] ($\mathrm{Re}_\tau = 235$) and Ghosh *et al.* [7] ($\mathrm{Re}_\tau = 245$), as displayed in Fig. 2(e). The present results and reference data in Figs. 2(c) and 2(e) demonstrate systematic deviations from canonical logarithm-law predictions: although van Driest transformed mean velocity profiles retain the classical logarithmic slope, the additive constant exhibits dependence on Reynolds and Mach numbers in channel and pipe flows [8,16]. In Fig. 2(f), the normal Reynolds stresses τ^+_{11} in the SP are in good agreement with the results of Modesti and Pirozzoli [16], while minor differences still exist between the other stresses and reference data. Therefore, the above accumulated evidence indicates that turbulence statistics obtained from the present computation have strong consistency with the established theoretical characteristics, and the developing flows in the CBL and SP exhibit a considerable degree of similarity to the fully developed flows in channels and pipes.

As illustrated in Fig. 3, the FBL is confined solely in the negative y-axial direction, while the CBL additionally incorporates the confinement in the positive y-axial direction, and the SP further imposes wall confinements in $\pm z$-axial directions. Based on the intensity of geometric confinements, the density increase of the core flow in the SP is the greatest, followed by that in the CBL. As the FBL has minimal mainstream compression effect, there only exists the density change due to the wall viscosity, which is why the van Driest transformation contributes the least to its maximum velocity.

To delineate the similarities and differences of these cases, a comparative analysis of zero-curvature boundary layers is performed as follows. As shown in the velocity profiles at the inlet [Fig. 4(a)], the u^+ curves reveal the wall-normal distributions of the mean velocity for planar flows (the FBL and CBL) share the common characteristics, while the pipe flow (the SP) exhibits gradually greater deviations starting from $y^+ \approx 20$. After the van Driest transformation, the $u^+_{\rm VD}$ curves indicate that the SP has the highest level of velocity, followed by that of the CBL, with the corresponding value of the FBL being the lowest. Referring to van Driest transformation, given that the fluid density on the wall $\bar{\rho}_w$ is almost fixed under the same inflow and wall conditions, the variations of the maximum velocity are resulted from the mean density $\bar{\rho}$ through the boundary layer. As the compressible flow transverses over the wall, the progressive development of the turbulent boundary layer causes a modest compression in the mainstream, with a corresponding increase in the density. Similarities and differences in the distribution of the root-mean square of velocity fluctuations $\langle u_i u_i \rangle^+_{\rm rms}$ and $\langle uv \rangle^+$ are depicted in Fig. 4(b). The peak positions and values of $\langle uu \rangle^+_{\rm rms}$ for the FBL, CBL, and SP are consistent. The outer region ($y^+ \gtrsim 100$) exhibits slightly higher levels of $\langle uu \rangle^+_{\rm rms}$, $\langle vv \rangle^+_{\rm rms}$, and $-\langle uv \rangle^+$ in the FBL compared to the corresponding fluctuations in the CBL and SP. This finding indicates that the presence of wall confinements may reduce velocity fluctuations to some degree. Furthermore, throughout all values of y^+, the FBL has the highest $\langle ww \rangle^+_{\rm rms}$, followed by the CBL, with the SP showing the lowest value, which strongly demonstrates the correlation between velocity fluctuations and geometric confinements, especially in the spanwise direction.

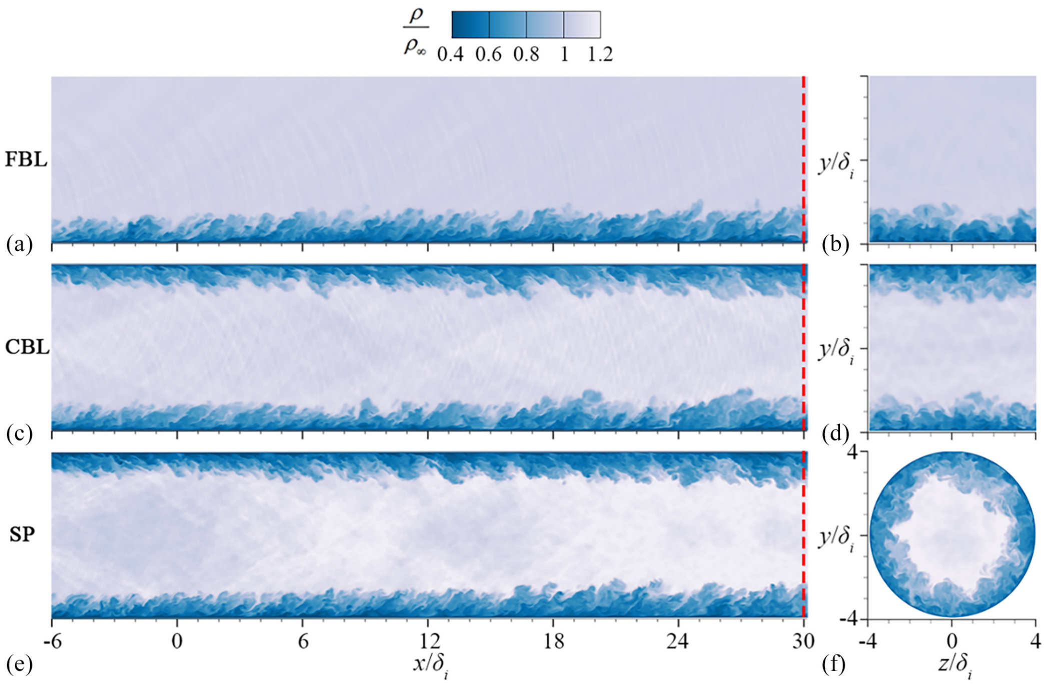

FIG. 3. Instantaneous density fields ρ/ρ_∞ on the (a), (c), (e) x-y planes and (b), (d), (f) cross-sectional slices in the (a), (b) FBL, (c), (d) CBL, and (e), (f) SP. The red dashed lines in (a), (c), and (e) indicate the slice positions in (b), (d), and (f), respectively.

As one of the crucial features of wall-bounded flows, low-speed streaks play a dominant role in the mass transport and momentum exchange between the inner and outer regions of the boundary layers [89,90]. To quantitatively study the spatial features of low-speed streaks, the relationship between the streak spacing and wall-normal distance is depicted in Fig. 5. In this study, data are

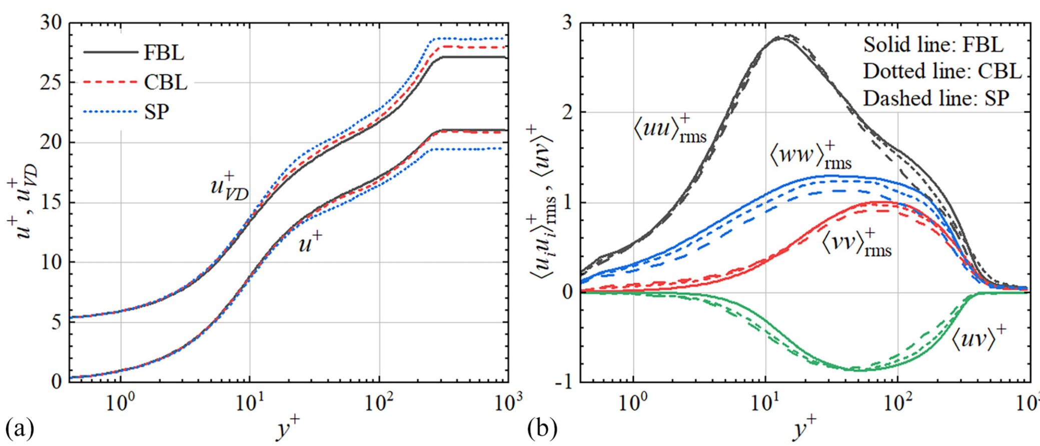

FIG. 4. Wall-normal distributions of (a) the mean velocity and van Driest transformed mean velocity (shifted upward by 5), and (b) the velocity fluctuations at the inlet of the critical simulation region in the FBL, CBL, and SP.

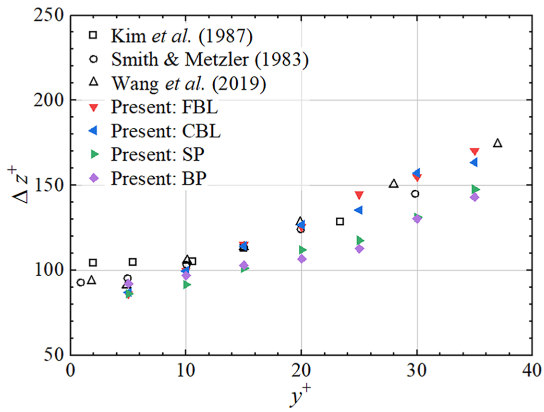

FIG. 5. The relationship between the streak spacing with the wall-normal distance at the inlet of the critical simulation region. Comparisons are made with the results of Kim *et al.* [91], Smith and Metzler [90], and Wang *et al.* [66].

recorded at intervals of 5 from $y^+ = 5$ to 35. For each y^+ location, individual streak spacings are identified and measured using an automated detection algorithm based on local velocity gradient thresholds. The comparison with the results of prior studies [66,90,91] demonstrates that the correlation between the streak spacing and the wall-normal distance in planar flows (the FBL and CBL) agrees well with the reference data because of the sufficiently large spanwise extent of the computational domain. However, the spacing of streaks in the SP and BP is first consistent within $y^+ \leqslant 10$, whereas it lags in the FBL and CBL, at least after $y^+ = 15$. As the distance from the wall increases, the streaks in the pipe flows become narrower than those in the planar flows owing to the spanwise confinement. The difference between the planar and pipe flows may consequently result in changes in the turbulence generation and transportation within the boundary layer. In light of the findings mentioned above, for the subsequent study of the BP, the SP will serve as a reference for comparison, in order to minimize the discrepancies induced by planar flows.

III. RESULTS AND DISCUSSION

A. Instantaneous and mean properties in supersonic bent pipes

To provide an overview of the flow phenomena in the BP, Fig. 6 visualizes vortices and shock waves in the supersonic flow field using the isosurfaces of the second eigenvalue of the velocity gradient tensor λ_2 [92] and the magnitude of density gradients.

Turbulent coherent structures within the boundary layer, such as hairpin vortices [93], are clearly identified in the figure. A dramatically thickening low-speed turbulent region is observed in the upper boundary layer, suggesting separation may occur at $x/\delta_i \approx 12$ on the convex wall. According to the classification of typical separation problems by Deck [94], when the boundary-layer thickness is considerably smaller than the offset height of streamlines, separation is primarily induced by the geometry or pressure gradient on the curved surface. Therefore, the geometry of the BP, particularly its curvature, provides a fundamental condition for the turbulent boundary layer separation, while the APG acts as the trigger. In the lower boundary layer, the distribution of vortices appears less dense in the downstream region than in the upstream region. Moreover, an oblique three-dimensional shock wave interacts with the turbulent boundary layer at the horizontal coordinate $x/\delta_i \approx 20$. A complex wave system also exists in the downstream region of the bend. To summarize, different responses of the boundary layers to the convex and concave curvatures are included in the bent pipe, and compressibility imparts more complexity to the flow field. The mechanisms underlying these phenomena are discussed below.

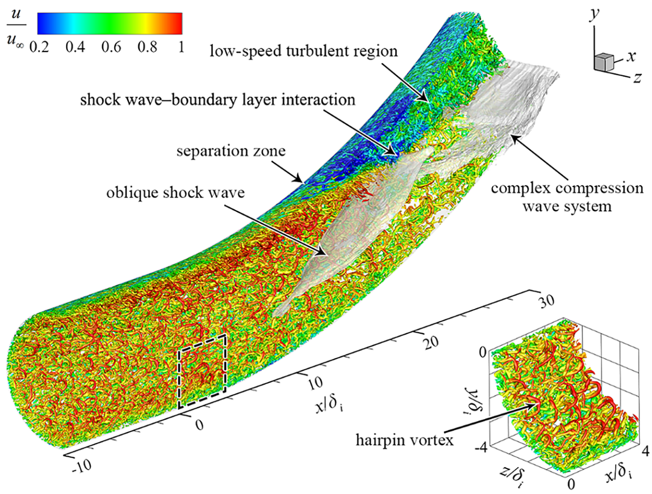

FIG. 6. Three-dimensional view of turbulence and wave structures in the BP. Instantaneous isosurfaces of $\lambda_2 = -1 \times 10^4$ colored by the streamwise velocity u/u_∞ are used to visualize the vortex field, where the region of $z/\delta_i > 0$ is excluded. Compression wave system is characterized by time-averaged isosurfaces of $|d\rho/dy| = 5$. The bottom-right subfigure provides an enlarged view of the region enclosed by the black dashed box.

Comparing Fig. 3, the observation of Fig. 7 displays the similar developing patterns of zero-curvature turbulent boundary layers in the range of $x/\delta_i < 0$, and also indicates that the boundary layer in the straight section upstream of the bend of the BP shares the consistent properties with the boundary layer in the SP. Nonetheless, owing to the involvement of the additional streamwise curvature, the density field in the pipe bend of the BP distinctly differs from that in the corresponding section of the SP. On the upper side, the low-density region within $3 \lesssim x/\delta_i \lesssim 15$ refers to the expansion of the core flow. These low-density fluids are exclusively present within the thickening boundary layer after $x/\delta_i \approx 15$, which is a typical view of turbulent boundary layer separation [95,96]. Furthermore, a notable increase in the density on the lower side of the BP is observed for both the mainstream and boundary-layer flows, indicating bulk compression effects. Evidently, the lower boundary layer thinned as the supersonic flow progressed downstream, which is a common response of the boundary layer to the concave curvature [43,97]. Therefore, based on the above

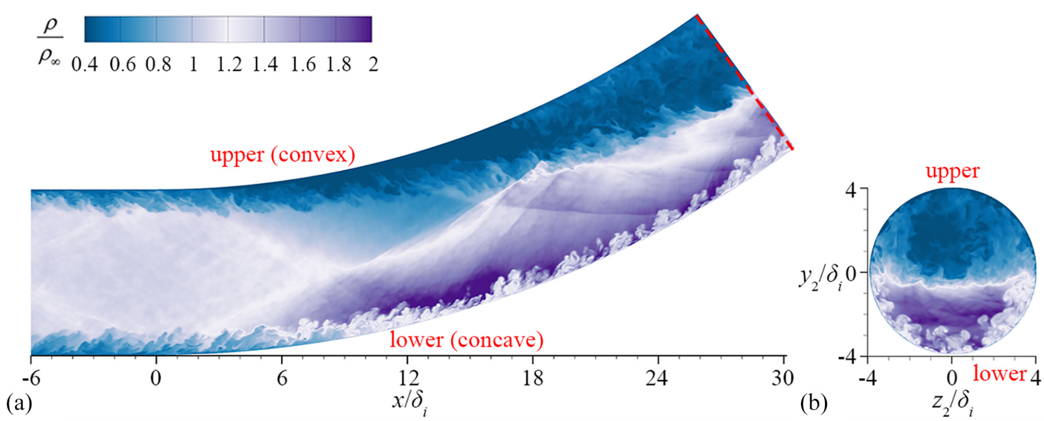

FIG. 7. Instantaneous density fields ρ/ρ_∞ on the (a) x-y plane and (b) cross-sectional slice in the BP. The red dashed line in (a) indicates the slice position in (b).

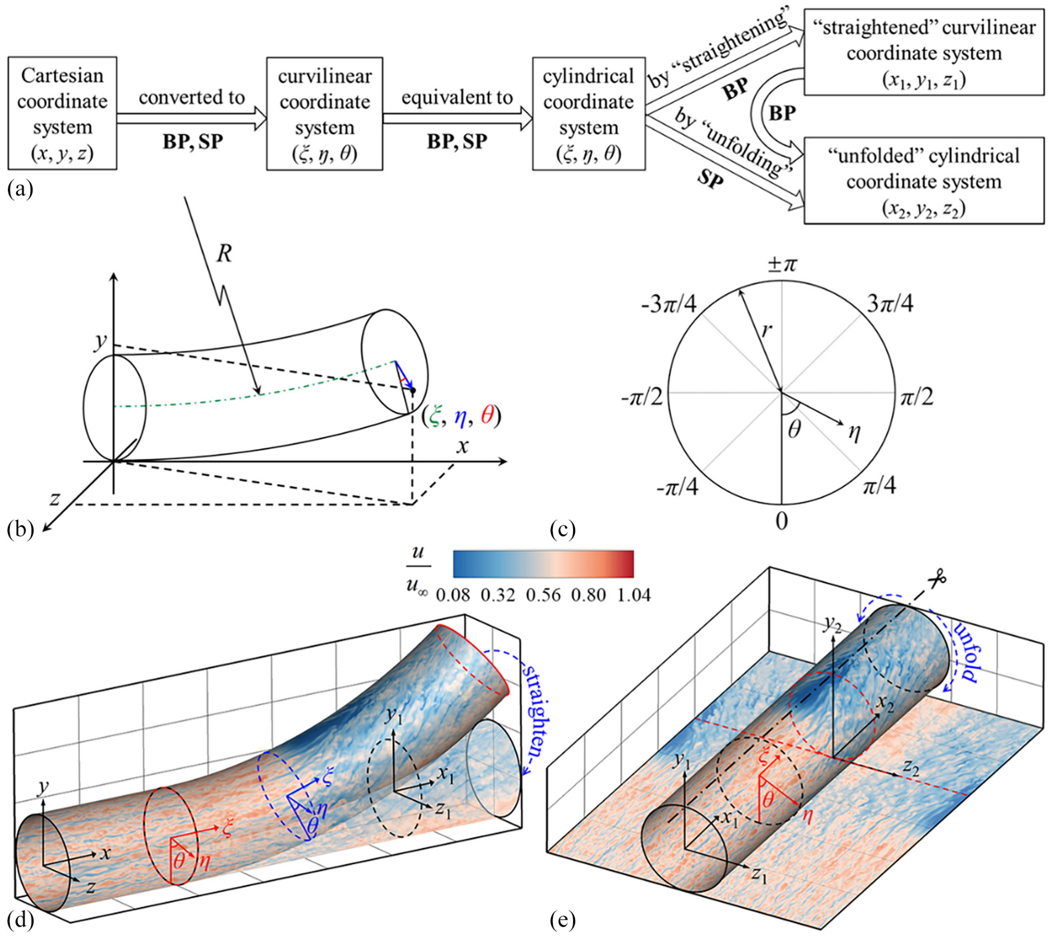

FIG. 8. Schematics of coordinate transformations in this study, including (a) the relationship of coordinate systems, (b) the descriptions in the Cartesian coordinate system and the curvilinear coordinate system, (c) the azimuthal distribution of θ in a circle, and processes of (d) "straightening" and (e) "unfolding," considering the velocity contours u/u_∞ of the BP as an example.

preliminary analysis, the different flow behaviors reflected on the upper and lower sides of the BP, including separation, compression and expansion effects, cause the varying growth trends of turbulent boundary layer on the upper and lower sides, eventually leading to the nonuniform phenomenon depicted in Fig. 7(b).

In this study, coordinate transformations are proposed to facilitate the observation and intuitive understanding of the flow fields within the pipes, to enable a direct comparison from a unified visual perspective between the SP and BP, and to allow for the convenient extraction and quantitative analysis of streamwise and circumferential boundary layer turbulence data, as depicted in Fig. 8(a). The first purpose is to "straighten" BP into the same configuration as SP. The conventional Cartesian coordinate system (x, y, z) can be converted to a curvilinear coordinate system (ξ, η, θ). Further, ξ represents the arc length of the centerline in the pipe bend, whereas η and θ denote the radial length and azimuthal angle on the cross section perpendicular to the centerline [see Fig. 8(b)]. To mark the azimuthal angle θ, this study adopts the range of $[-\pi, \pi]$ (in rad), starting from the upper point (the top point of the circular cross section) and increasing in the counterclockwise direction, as shown in Fig. 8(c). The relationship between them can be described as

$$x = (R + \eta\cos\theta)\sin\alpha, \quad y = R(1 - \cos\alpha) - \eta\cos\theta\cos\alpha, \quad z = \eta\sin\theta, \tag{4}$$

where α indicates the bending angle, which is defined as the quotient of the arc length and radius of the curvature circle, that is, $\alpha = \xi/R$.

The curvilinear coordinate system is equivalent to a cylindrical coordinate system without any changes. The cylindrical coordinate system (ξ, η, θ) is reprojected into the orthogonal coordinate system, obtaining the "straightened" curvilinear coordinate system (x_1, y_1, z_1) as illustrated in Fig. 8(d). The transformation is written as follows:

$$x_1 = \xi, \quad y_1 = -\eta\cos\theta, \quad z_1 = \eta\sin\theta. \tag{5}$$

Thus, the bent section of BP can be transformed into the geometry of SP. However, it must be acknowledged that this spatial region would experience deformation, given that the upper arc length is consistently shorter than the lower arc length. This transformation is unnecessary for SP because the coordinates do not change at all. As shown in Fig. 8(e), by cutting along the top line of the cylindrical surface, the surface with a specific wall-normal distance can be spread out like a piece of roll paper. The above concept of "unfolding" can be applied to both SP and straightened BP. Based on this approach, the cylindrical coordinate system can be mapped onto the unfolded coordinate system (x_2, y_2, z_2), with

$$x_2 = \xi, \quad y_2 = r - \eta, \quad z_2 = r\theta, \tag{6}$$

where x_2 denotes the streamwise distance in the direction tangent to the curvature wall, y_2 is equivalent to the wall-normal height y_w, and z_2 is associated with the azimuthal angle θ. This coordinate system enables to view the boundary layer in the pipe as that on a plane. The primary objective of the aforementioned coordinate transformations is merely to facilitate optimized visualization of turbulent boundary layers in the bent pipe. Unless specifically stated, flow parameters are maintained invariant under these transformations in the subsequent investigation.

By employing coordinate transformations, the mean flow field obtained in the upper and lower regions of the BP is compared with the corresponding data in the SP. Following the van Driest transformation, the wall-normal distributions of the mean velocity and velocity deficit are examined simply at the three key locations: the start ($x_1/\delta_i = 0$), midpoint ($x_1/\delta_i = 15$), and termination ($x_1/\delta_i = 30$) of the critical simulation region, as shown in Fig. 9. The van Driest transformed mean velocity profiles of $x_1/\delta_i = 15$ and 30 achieve higher u^+_{VD} within $y^+ \lesssim 20$ compared to those of the SP, and their peak velocities gradually decrease with the streamwise distance. Meanwhile, the velocity deficit of $x_1/\delta_i = 30$ exhibited an acceleration of zero in the boundary layer. These situations indicate that the compression in the lower region thins the turbulent boundary layer and reduces the mainstream velocity. A backflow is present near the upper wall in the BP, which is depicted by the occurrence of negative streamwise velocity within $y^+ \lesssim 80$ at $x_1/\delta_i = 15$. It is a typical indicator of boundary-layer separation, wherein the downstream flow velocity reverses direction and causes the upstream boundary-layer flow to be lifted away from the wall. In contrast, the velocity for $y^+ \gtrsim 600$ at $x_1/\delta_i = 15$ reaches a higher level than that in the SP, which is attributed to the expansion effect discussed previously. Moreover, the reduction in the van Driest transformed mean velocity of $x_1/\delta_i = 30$ and the corresponding velocity deficit suggest that the low-speed turbulent region in the upper boundary layer continuously expands along with the streamwise distance.

To further evaluate the extent to which compressibility affects the development of boundary layers, the distributions of mean density and temperature at the same three locations were examined, as shown in Fig. 10. The results indicate that in the SP, both the mean density and temperature change gradually with the wall-normal height. In contrast, the bent-pipe flow exhibits pronounced variations on both the upper and lower sides. On the lower side of the BP, the mean density increases more rapidly away from the wall compared to the SP, while the opposite trend is observed on the upper side. Notably, at $x_1/\delta_i = 15$ within the upper boundary layer, the mean density remains nearly

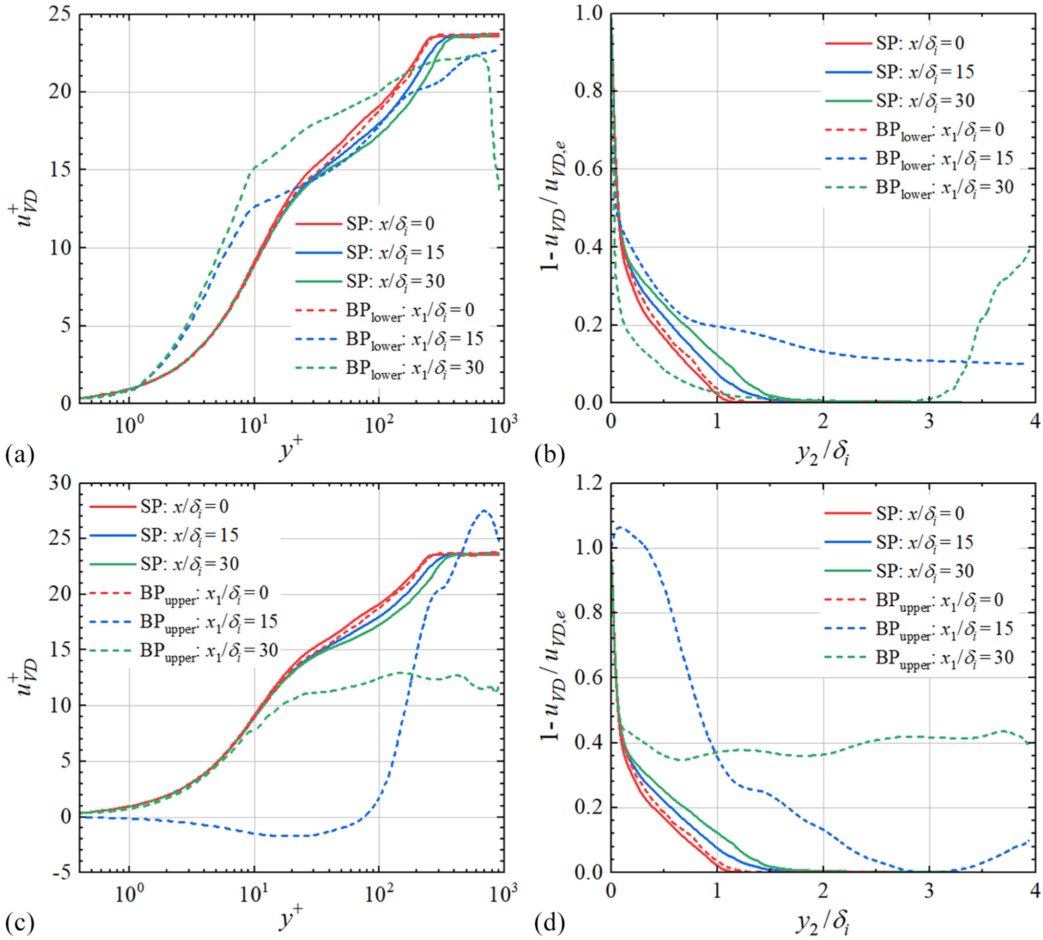

FIG. 9. Wall-normal distributions of (a), (c) the van Driest transformed mean velocity u^+_{VD} as the function of y^+ and (b), (d) the velocity deficit $(1-u_{\mathrm{VD}}/u_{\mathrm{VD},e})$ as the function of y_2/δ_i at different streamwise positions, including $x_1/\delta_i = 0$, 15 and 30, with comparisons (a), (b) between the SP and the lower region of the BP, and (c), (d) between the SP and the upper region of the BP.

constant relative to the wall value for $y^+ \lesssim 80$. This region coincides with the backflow found in Fig. 9, suggesting that density basically remains unchanged inside the separation zone. Moreover, the rate at which temperature decreases with the wall-normal height correlates with the rate of density increase. Overall, the influence of flow compressibility on the boundary layer is summarized as an increase in density due to compression on the lower wall and a decrease in density due to expansion on the upper wall, which significantly make impacts on the velocity profile and deficit analyzed earlier.

To quantitatively delineate the development between the upper and lower boundary layers, Fig. 11 illustrates the streamwise velocity $u_n = u\cos\beta + v\sin\beta$, the pressure p, and their gradients at different wall-normal heights in the BP. According to Eq. (5), negative y_1 corresponds to the lower side and positive y_1 corresponds to the upper side. Evidently, the flow velocity on the upper side immediately drops downstream, indicating a significant impact of separation on the boundary layer. Backflow is also observed in the streamwise range $12 \lesssim x_1/\delta_i \lesssim 18$ on the upper wall. In addition, the lower boundary-layer flow experiences a positive $\mathrm{d}p/\mathrm{d}x_1$ (APG) after entering the bent section but encounters a negative $\mathrm{d}p/\mathrm{d}x_1$ (FPG) within $14 \lesssim x_1/\delta_i \lesssim 24$. Conversely, the upper

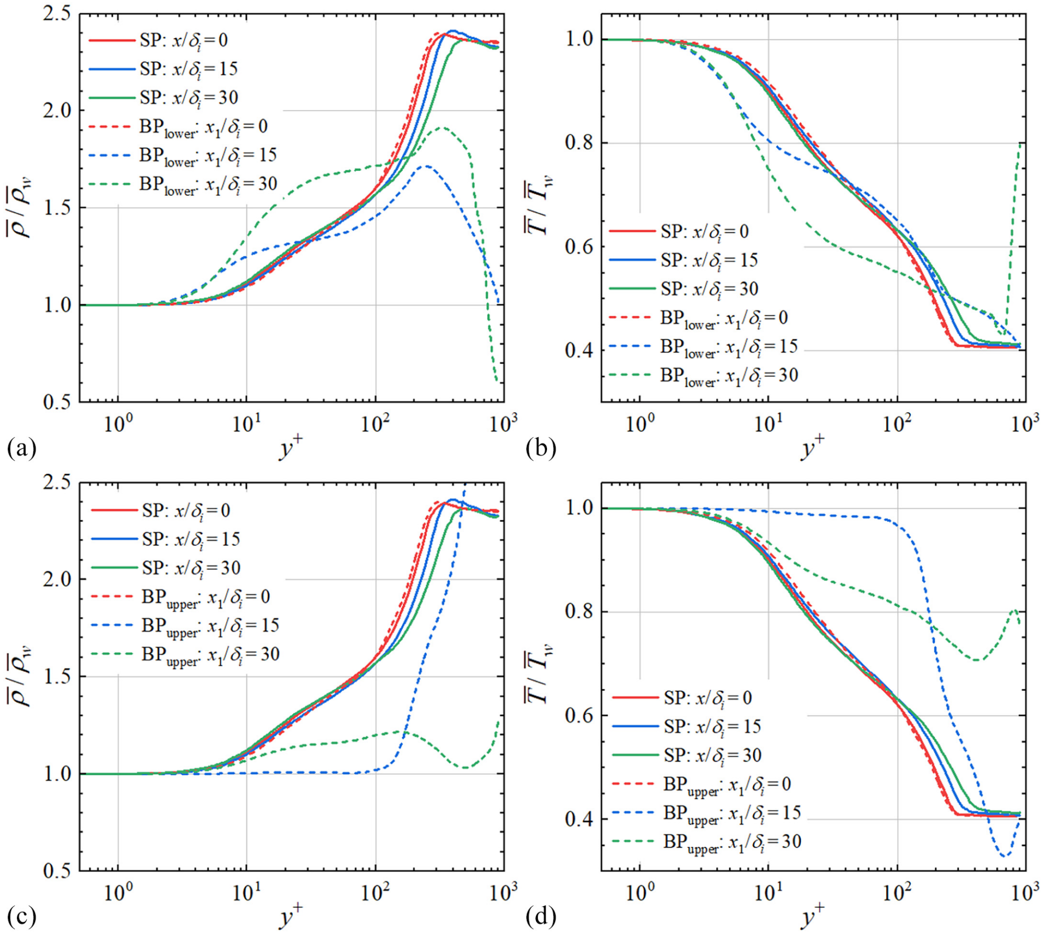

FIG. 10. Wall-normal distributions of (a), (c) the mean density $\bar{\rho}/\bar{\rho}_w$ and (b), (d) the mean temperature $\bar{T}/\bar{T}_w$ as the function of y^+ at different streamwise positions, including $x_1/\delta_i = 0$, 15 and 30, with comparisons (a), (b) between the SP and the lower region of the BP, and (c), (d) between the SP and the upper region of the BP.

boundary-layer flow is initially affected by the FPG, and is influenced by the APG in the local region of $11 \lesssim x_1/\delta_i \lesssim 24$. These findings reveal that the variations of pressure in the flow field of the BP are closely associated with the curvature of the wall surface, as the concave curvature induces the APG and the convex curvature typically induces the FPG. Meanwhile, a strong correlation between the velocity gradient and pressure gradient can be found in the near-wall region ($y_1/\delta_i = -3.9$ and 3.9). Specifically, the local FPG is related to the deceleration of the fluid near the wall, whereas the local APG is associated with acceleration, which is consistent with the theory of extra strain rates proposed by Bradshaw [37]. Consequently, the APG and the decreasing velocity collectively induce separation in the upper turbulent boundary layer.

Therefore, the pressure gradient along the streamwise direction varies in local regions. The flow field exhibits ZPG-FPG-APG and ZPG-APG-FPG distributions on the upper and lower sides, respectively. According to Simpson [95], a rapid change in surface curvature can also lead to insufficiently curved streamlines, allowing the generation of separated flows within the APG region. When the boundary layer is subjected to the APG, accompanied by the flow deceleration, the boundary layer tends to become separated. On the upper side of the BP, the convex wall can naturally reduce the streamwise flow speed and even generate reverse flow, and combined with the

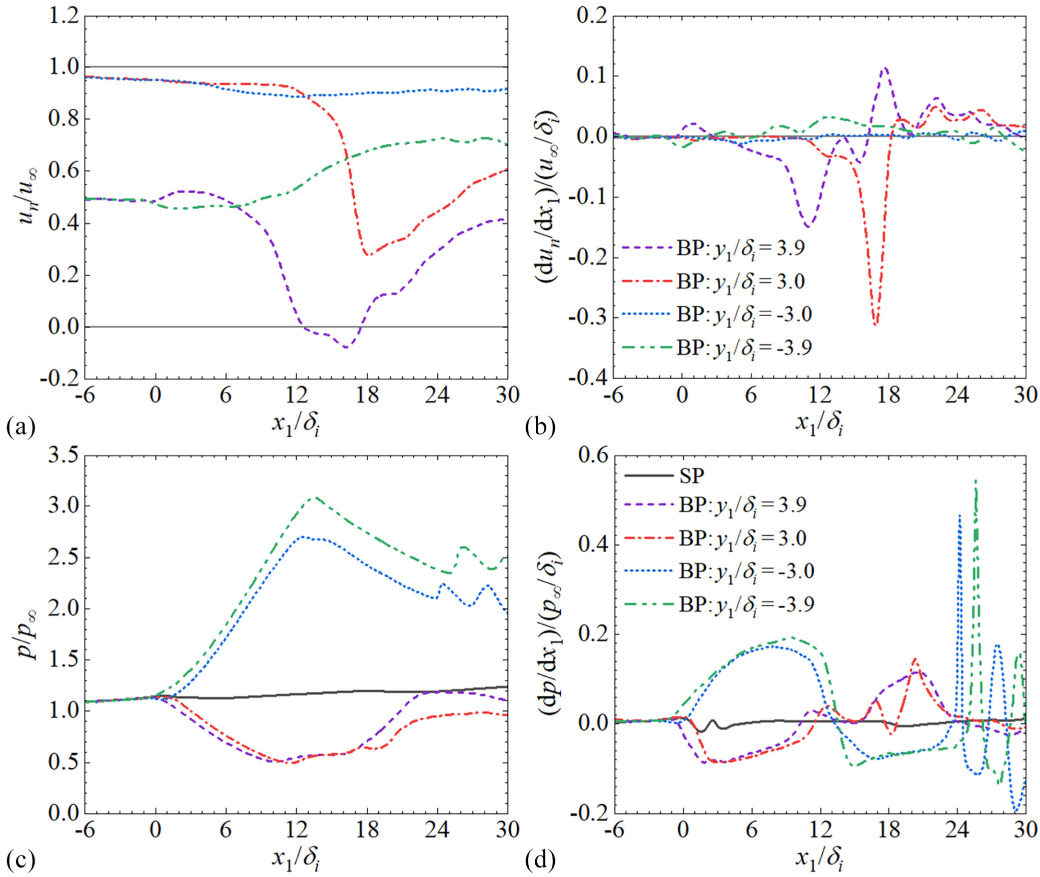

FIG. 11. Streamwise distributions of (a) the velocity component u_n/u_∞, (b) the velocity gradient $(\mathrm{d}u_n/\mathrm{d}x_1)/(u_\infty/\delta_i)$, (c) the pressure p/p_∞, and (d) the pressure gradient $(\mathrm{d}p/\mathrm{d}x_1)/(p_\infty/\delta_i)$ at different radial positions in the BP, including $y_1/\delta_i = 3.9$, 3.0, -3.0, and -3.9.

influence of the local APG, these factors provide the fundamental conditions for flow separation. Conversely, on the lower side, Xu and Wu [48] also explained that the existence of streaks or Görtler vortices on the concave surface was able to suppress separation by changing the mean flow profile. In addition to the curvature of the bent pipe in this study ensuring that the streamlines adapt to the wall, the Görtler instability contributes to the reorganization of the turbulence, thereby preventing the lower boundary layer from separating in the APG region. Furthermore, the large oscillation of the pressure gradients for $x_1/\delta_i \gtrsim 24$ contributes to the influence of shock waves, as explained in the subsequent description. Because of the sensitivity of the flow-field data to waves, qualitative analyses are performed for this complex region, as described in the following section.

Figure 12 shows the mean statistics of velocity and pressure in the BP, clearly illustrating the flow field from the beginning to the end of the bend. To facilitate the following analysis, the approximate locations of the separation (recirculation) zone are noted in the contours based on the region with negative velocity, and compression and expansion waves are sketched according to the spatial distribution of the mean pressure and density, as visually demarcated by colored auxiliary lines. These schematic approaches contribute to a more comprehensive understanding of the flow phenomena. Backflow is also observed in the inner region of $12 \lesssim x_1/\delta_i \lesssim 18$ on the

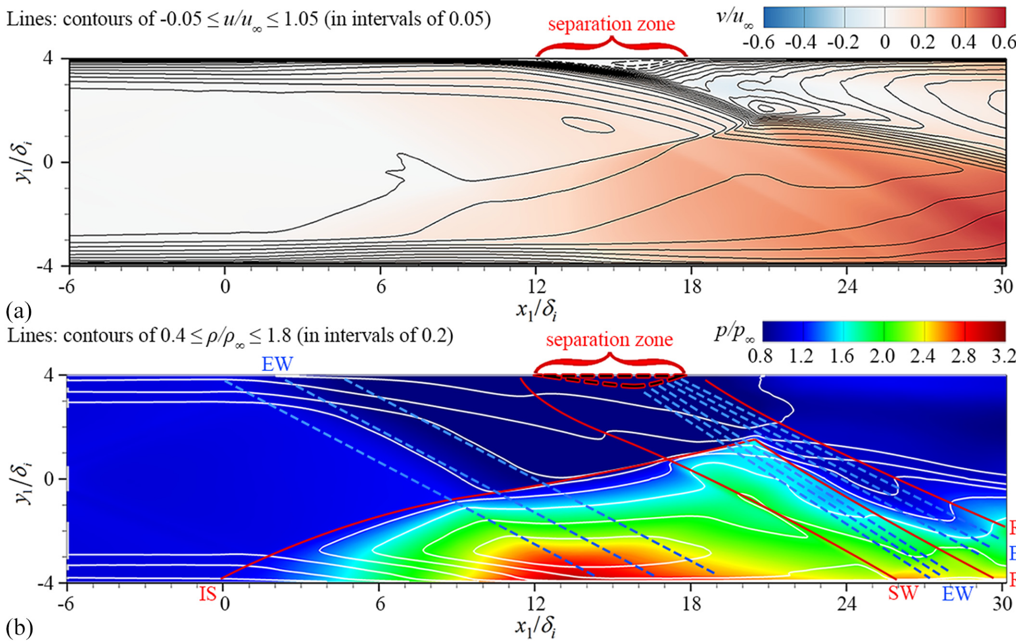

FIG. 12. Time-averaged (a) velocity field v/u_∞ and (b) pressure field p/p_∞ on the x_1-y_1 slice in the BP. The black lines in (a) identify contours of u/u_∞ ranging from -0.05 to 1.05 in intervals of 0.05, where the solid lines denote positive values, and the dashed lines denote zero and negative values. The white solid lines in (b) identify contours of the normalized density ρ/ρ_∞ ranging from 0.4 to 1.8 in intervals of 0.2, and the sketch curves include red solid lines indicating compression waves and blue dashed lines indicating expansion waves. The red brace indicates a separation (recirculation) zone. Abbreviations in the figure: IS, incident shock; RS, reflected shock; EW, expansion waves; SW, separation shock wave; RW, reattachment shock wave.

upper side, which is consistent with the previous discussion. The occurrence of backflow does not necessarily indicate separation, even though the separated boundary layer is frequently accompanied by the recirculation zone [96]. The qualitative insights from Figs. 6 and 7, in conjunction with the quantitative evidence depicted in Fig. 13, confirms the occurrence of separation in this region.

The pressure field shown in Fig. 12(b) identifies a series of expansion waves on the upper side of the BP as the boundary-layer flow enters the bend. Moreover, the oblique compression wave originates from the pressure variations on the lower wall and serves as the incident shock that interacts with the upper boundary layer at the streamwise coordinate $x_1/\delta_i \approx 20$. The reflected shock wave, which is coincidentally sandwiched in the middle of the expansion fan generated near the separation zone, is clearly captured. Additionally, two compression waves, known as separation and reattachment shock waves, are present at both the leading and trailing edges of the separation zone. The formation of these waves has been well explained by the theoretical studies of canonical shock-wave–boundary-layer interactions [98,99]. Based on the streamwise distribution of the pressure gradients shown in Fig. 11(d). The interaction of the shock wave and the boundary layer leads to a notable pressure rise on the upper wall, resulting in the local APG region of $11 \lesssim x_1/\delta_i \lesssim 24$. Similarly, the expansion waves originating from the upstream upper region also have a pressure-lowering effect on the downstream lower region, forming the FPG locally. In addition, the velocity direction of the core flow is also altered by the interplay of compression and expansion waves, reflected from the phenomenon that the mainstream velocity component v at the outlet ($x_1/\delta_i \approx 30$) is greater than that at the inlet ($x_1/\delta_i = 0$). However, shock waves in bent

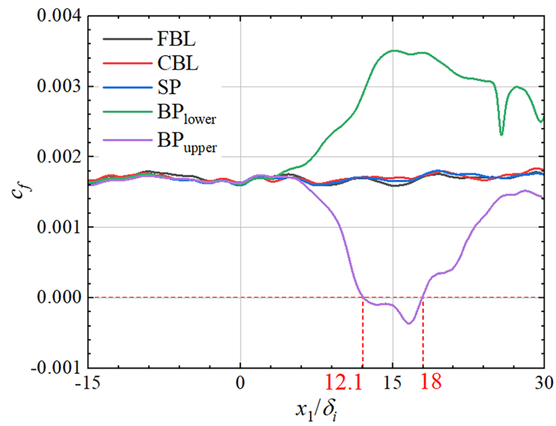

FIG. 13. Streamwise distribution of the skin friction coefficient c_f in the FBL, CBL, SP, and BP. Here, the statistics of the BP are obtained on both the upper and lower walls.

pipes exhibit complex three-dimensional structures (see Fig. 6); therefore, the above analysis could overlook the three-dimensional effects of shock-wave–boundary-layer interactions.

To compare the effects of the curvature on boundary layers of different cases, Fig. 13 illustrates the distribution of the skin friction coefficient $c_f = 2\bar{\tau}_w/\rho_\infty u_\infty^2$ along the streamwise distance, which is derived from the shear stress on the wall ($\bar{\tau}_w = \bar{\mu}_w \mathrm{d}\bar{u}/\mathrm{d}y_w$). For the zero-curvature boundary layers, including the FBL, CBL, and SP, the friction coefficient climbs slowly, indicating an overall average level of 0.0017. The skin friction from the lower wall of the BP is strengthened when the flow entered the pipe bend. This increase is not only a response to the rising pressure and density on the lower side of the BP, but also a manifestation of the large-scale motion within the boundary layer on the concave wall [44,66]. By contrast, the wall shear friction on the upper side first drops below zero and then rebounds above zero, which represents the process of flow separation and reattachment within the turbulent boundary layer. The separation and reattachment points, which together determine the extent of the separation zone, are located at $x_1/\delta_i = 12.1$ and 18.0 on the upper wall, respectively.

In addition to the analysis of streamwise and radial statistics, the spanwise characteristics of the flow field in the BP are delineated as follows. As depicted in Figs. 14(a)–14(c), the vorticity field displays reverse symmetry across the left and right sides as well as an enhancement of the streamwise vorticity component ω_{x_n} in the incipient separation on the upper wall. As described by Krishna *et al.* [96], secondary flow is induced by the imbalance between the centrifugal force and radial pressure gradients and also has a promoting effect on separation in the BP. The pressure fields shown in Figs. 14(d)–14(f) indicate the correlation with the formation of Dean vortices because the secondary motion in the boundary layer is related to the circumferential distribution of pressure gradients [33]. The same as those classical Dean vortices observed in incompressible bent pipes [24], the quantitative and qualitative evidence demonstrates that secondary flows exhibit a pair of large-scale, counterrotating, and symmetric vortices in the compressible bent pipe investigated. In the circumferential boundary layer, the presence of secondary flows can promote transport of mass and energy [32]. The vorticity is known as the curl of the velocity vector, the component of which in the ith direction is denoted as ω_{x_i} here. The spanwise distributions of the vertical velocity component $v_n = v\cos\beta - u\sin\beta$ and streamwise vorticity component $\omega_{x_n} = \omega_x \cos\beta + \omega_y \sin\beta$ (see Fig. 15) exhibit symmetry on the left and right sides of the cross sections. Except for the slice at $x_1/\delta_i = 0$, every other slice shows a positive v_n near the wall, whereas the core flow is motivated in the opposite direction driven by the centrifugal force. Similarly, slices apart from $x_1/\delta_i = 0$ indicate clockwise vortices in the negative z_1 region and counterclockwise vortices in the positive z_1 region, respectively.

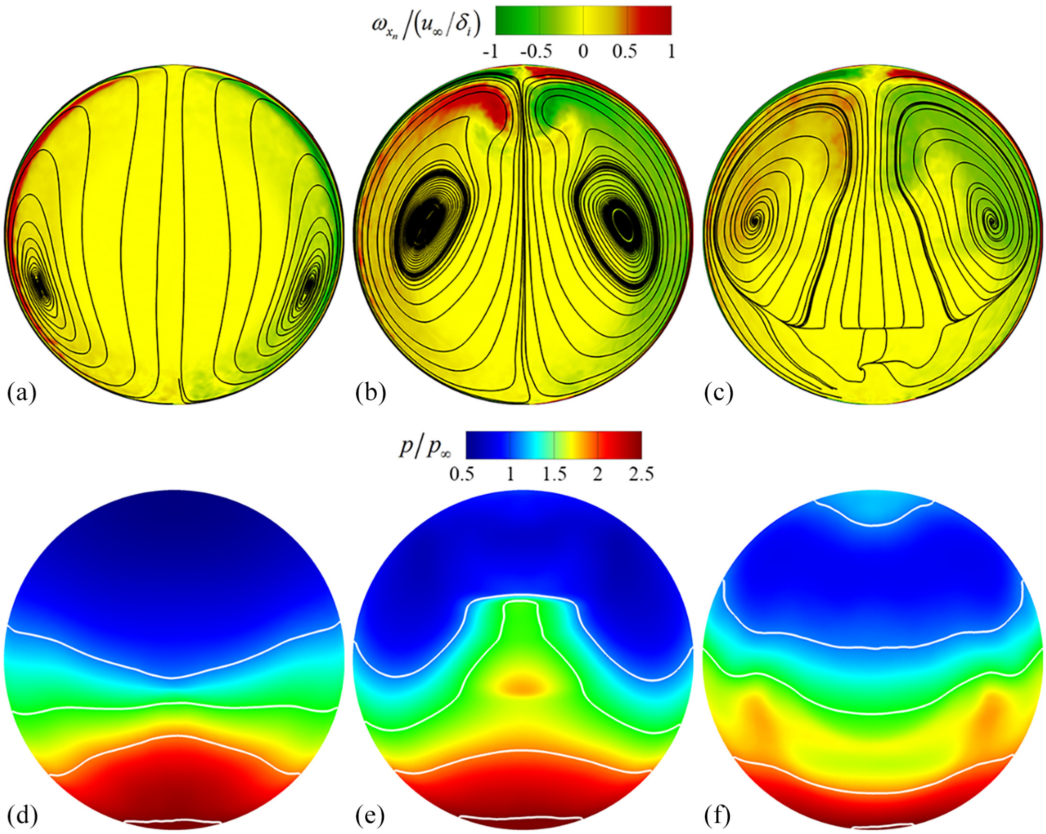

FIG. 14. Time-averaged contours of (a)–(c) the vorticity component $\omega_{x_n}/(u_\infty/\delta_i)$ and (d)–(f) the pressure p/p_∞ at different streamwise positions in the BP, including $x_1/\delta_i =$ (a), (d) 10, (b), (e) 20, and (c), (f) 30. The black solid lines in (a)–(c) represent the streamlines perpendicular to the primary flow direction, and the white solid lines in (d)–(f) identify contours of p/p_∞ ranging from 1 to 2.5 in intervals of 0.5.

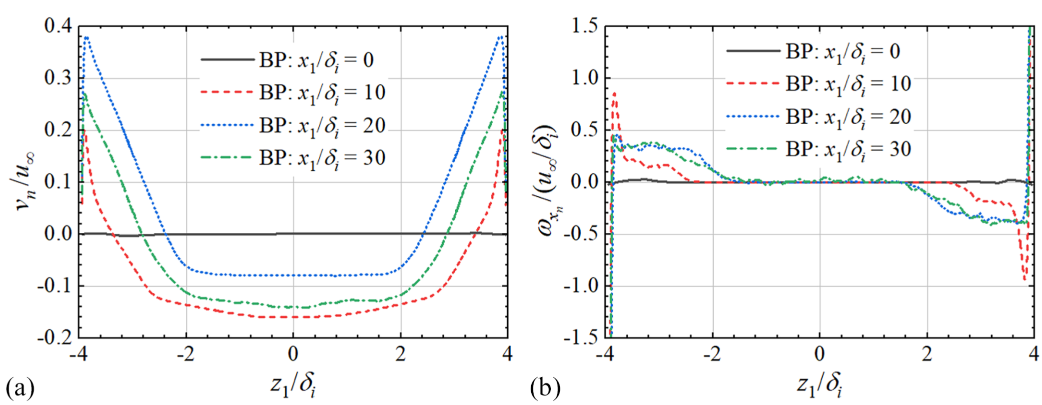

FIG. 15. Spanwise distributions of (a) the velocity component v_n/u_∞ and (b) the vorticity component $\omega_{x_n}/(u_\infty/\delta_i)$ at different streamwise positions in the BP, including $x_1/\delta_i = 0$, 10, 20 and 30.

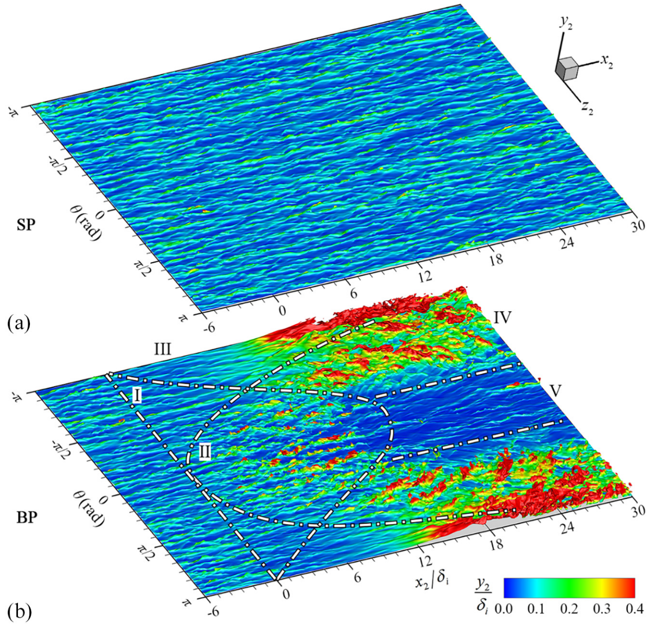

FIG. 16. Instantaneous isosurfaces of $u/u_\infty = 0.5$ in the (a) SP and (b) BP, colored by the wall-normal distance y_2/δ_i. The region $y_2/\delta_i > 1$ is excluded to clearly visualize the flow field. The white dotted-dashed line denotes the approximate boundaries of regions I–V within the boundary layer of the BP.

Figure 16 further illustrates the instantaneous characteristics of velocity field, where the isosurfaces of $u/u_\infty = 0.5$ are colored by the local wall-normal height. For the convenience of comparison, the approximate boundaries are delineated to indicate where expansion and compression waves originate at the inlet of the bend, and regions I–V exhibit their unique local characteristics based on their positions. Specifically, the schematic of the spatial distributions of compression and expansion waves has been detailed previously in Fig. 12. Evidently, the leading edge of the region I corresponds to the position $x_2/\delta_i = 0$. The boundary between regions I and II indicates that the region downstream is the influence domain of compression waves, whereas the boundary between regions I and III demonstrates that the region downstream falls within the influence domain of compression waves. Furthermore, regions IV and V are distinguished primarily by their angular ranges, but they display different spatial distributions of boundary-layer fluids at the same flow velocity. A comparison between the SP and the BP clearly indicates that in the region II, some flow structures originating close to the wall are lifted up due to disturbances, and these disturbances appear to have wavelengths larger than the streak spacing in the upstream straight section, which may correspond to the existence of large-scale vortical structures. In addition, the effects of separation and shock-wave–boundary-layer interaction are responsible for the abundant protruding structures in regions III and IV. Meanwhile, variations in the boundary-layer thickness along the streamwise distance are clearly visible in the figure. For example, the thickening process in the region III and the thinning process in the region V are highlighted by color representation. While the instantaneous flow field provides valuable qualitative insight, it cannot conclusively demonstrate the coherent structures in boundary layers.

To clarify whether changes occur in flow patterns in the lower boundary layer, the lower region of the BP is laid emphasis in the following analysis. The time-averaged velocity fields (see Fig. 17) reveal noticeable differences in the lower boundary layer of the BP compared to that of the SP. Along the streamwise direction, the boundary layer in the SP experiences a minimal increase in thickness, represented by the 99% free-stream velocity, whereas the mainstream velocity remains

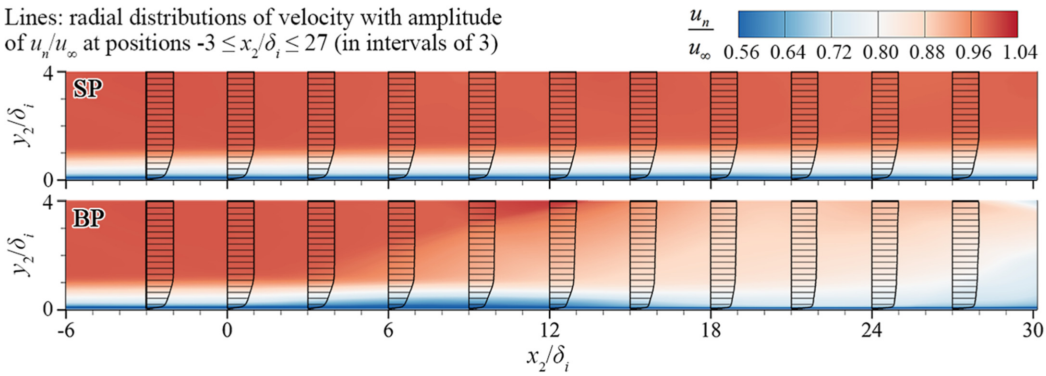

FIG. 17. Time-averaged velocity fields u_n/u_∞ on the x_1-y_1 slice in the SP and the lower region of the BP. The lines display radial distributions of u_n/u_∞ at different streamwise positions x_1/δ_i ranging from -3 to 27 in intervals of 3.

essentially constant. The lifting of the low-speed fluid in the lower region of $0 \lesssim x_1/\delta_i \lesssim 15$ of the BP may indicate the increasing Görtler instability. Further downstream ($x_1/\delta_i \gtrsim 18$), the boundary-layer thickness gradually decreases, falling below that of the corresponding position in the SP. The phenomenon may result from the reduction of the Görtler instability, the conversion from APG to FPG, and the invasion of the high-speed core flow into the lower region due to centrifugal forces. Moreover, at the outlet of the bend, the mainstream velocity is apparently lower than that at the inlet, which can be attributed to compression effects.

To quantitatively characterize the development of the lower boundary layer in the BP, the thickness of the lower boundary layer is necessary to be evaluated. Fernholz and Finley [100] critically noted that significant wall-normal variations in static pressure can alter the velocity profile, making the traditional criterion $u = 99\% u_\infty$ less applicable. Alternatively, Wang *et al.* [66] proposed a new definition of the mean principal strain rate $S_{\text{prin}} = \partial(u_n/u_\infty)/\partial(y/\delta_i)$ and successfully applied it to a supersonic boundary layer on a concave surface, and the threshold $S_{\text{prin}} = 0.08$ is adopted instead of the 99% boundary-layer thickness, as shown in Fig. 18(a). Additionally, the displacement thickness $\delta^* = \int_0^h [1-(\bar{\rho}/\bar{\rho}_e)(\bar{u}/\bar{u}_e)]dy$ and the momentum thickness $\theta^* = \int_0^h [(\bar{\rho}/\bar{\rho}_e)(\bar{u}/\bar{u}_e)(1-\bar{u}/\bar{u}_e)]dy$ are obtained to illustrate the mass and the momentum deficits within the compressible boundary layer. These two criteria are exhibited in Figs. 18(b) and 18(c), respectively. Hereinafter, the superscript "*" denotes the local parameter. To reduce the impact of fluctuations in the free-stream variables, such as $\bar{u}_e$ and $\bar{\rho}_e$, this study integrates up to a wall-normal height of $h = 1.5\delta_i$. The shape factor $H = \delta^*/\theta^*$ indicates the fullness of the mean velocity profile of the boundary layer, following the interpretation by Sun *et al.* [39], which is displayed in Fig. 18(d).

The contour of S_{prin} decreases in height from the wall at the inlet until the flow arrives at $x_1/\delta_i \approx 24$, suggesting that the outer limit of the boundary layer continues to move closer to the concave surface. This trend is independent of the internal variations within the turbulent boundary layer. The boundary-layer displacement thickness along the streamwise direction begins to decrease shortly after entering the bent section, and then increases again around $x_1/\delta_i \approx 15$. In contrast, the momentum thickness in the lower region of the BP exceeds that at the equivalent position in the FBL, CBL, and SP within $0 < x_1/\delta_i \lesssim 15$, followed by a decrease until $x_1/\delta_i \approx 24$. The streamwise distribution of the shape factor in the BP is lower than in other cases, indicating that the mean velocity profile in the lower boundary layer exhibits greater fullness compared to zero-curvature boundary layers. Therefore, the phenomena depict that the mass deficit is reduced, while the momentum deficit increases, which strongly demonstrate the Görtler instability rises in the lower boundary layers.

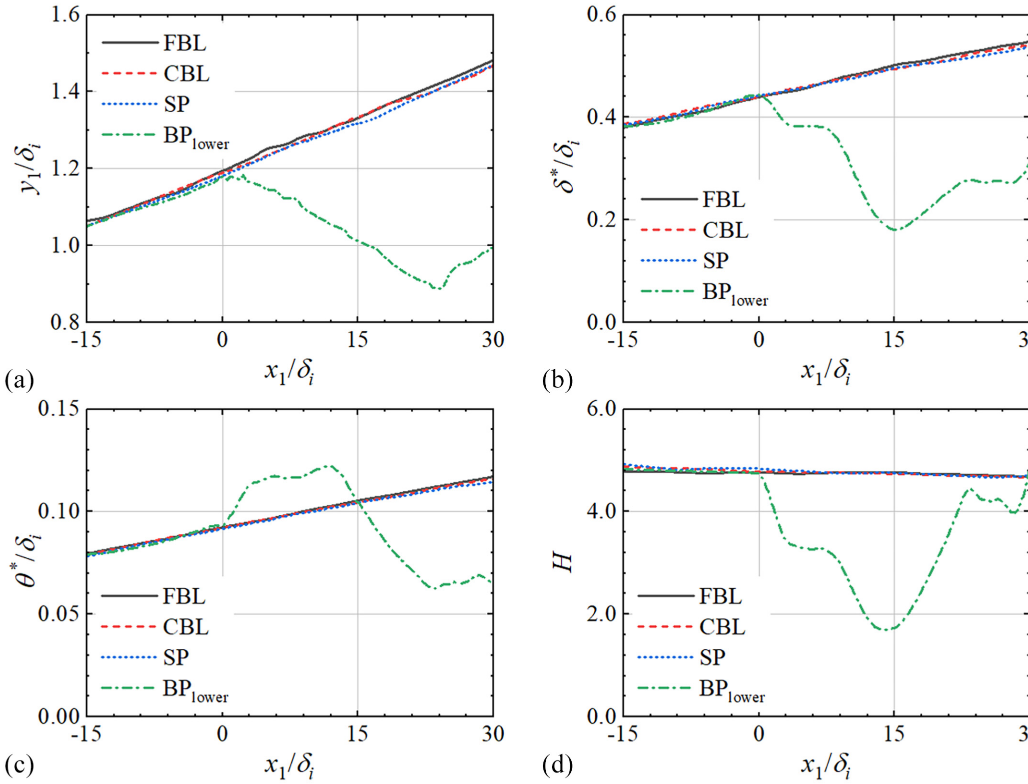

FIG. 18. Streamwise distributions of (a) the contour of the mean principal strain rate $S_{\mathrm{prin}} = 0.08$, (b) the displacement thickness δ^*, (c) the momentum thickness θ^*, and (d) the shape factor H for the boundary layer in the FBL, CBL, SP, and BP. Here, the statistics of the BP are obtained in the lower region.

B. Görtler instability in turbulent boundary layers

Görtler [45] introduced a dimensionless number to measure the centrifugal instability in laminar incompressible boundary layers. For turbulent compressible scenarios, the Görtler number is generally estimated as the following definition [52,54,57,58]:

$$G_T = \frac{\theta^*}{0.018\delta^*}\sqrt{\frac{\theta^*}{R^*}}, \tag{7}$$

where the radius of the local curvature circle is defined as $R^* \equiv R + r$. As reviewed by Xu *et al.* [60], G_T is a necessary indicator to study the excitation and downstream development of Görtler vortices. In this study, the Görtler number measured in the lower boundary layer satisfies $G_T > 1.6$, which is above the critical threshold of 0.6 proposed by Görtler [101]. Another criterion for evaluating the significance of streamline curvature, proposed by Floryan [51], is defined as δ_0^*/R^*, where δ_0^* denotes the local boundary-layer thickness. It has been applied to several investigations on supersonic flows (e.g., Refs. [57,58]). From the computation, there are $\delta_0^*/R^* \geqslant 0.016$ throughout the lower boundary layers, and especially $\delta_0^*/R^* > 0.02$ in the APG region. The results are much higher than the critical threshold of 0.01 established by Floryan [51]. These aforementioned two indicators suggest the occurrence of the Görtler instability in the lower turbulent boundary layer of the BP.

Classical Görtler vortices are frequently observed during the transition from laminar to turbulent flows. Floryan [51] theoretically predicted the emergence of Görtler-type vortices in turbulent boundary layers; however, either experimentally or numerically, identifying these structures poses

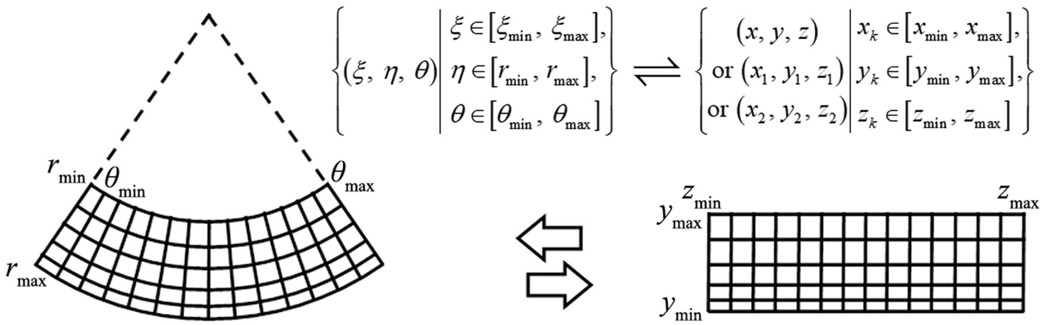

FIG. 19. Schematic of conditional spatial averaging.

significant difficulties due to the highly irregular and chaotic nature of the turbulent background. Up to now, extracting Görtler vortices from the abundant small vortices in the turbulent boundary layer is still challenging [102]. While the time-averaged statistics can measure the increase or decrease in the boundary-layer thickness, they do not provide the relevant information for the large-scale vortical structures because the fluctuations and critical flow structures are often obscured after long-term averaging [58]. To obtain more information of the Görtler instability, a conditional averaging technique is used to solve the above contradiction, which involves independent averaging in both the temporal and spatial aspects. First, a moderate duration is selected for conditional temporal averaging to avoid the randomness or elimination of fluctuations, which is $60\delta_i/u_\infty$, equivalent to just two flow-through times. The conditional temporal average result is expressed as

$$\widetilde{f}(\mathbf{x}) = \widetilde{f(\mathbf{r})}, \tag{8}$$

where f represents any one of flow variables, while $\mathbf{x}$ and $\mathbf{r}$ are the coordinate points used for the conditional spatial averaging introduced below.

As depicted in Fig. 19, the conditional spatial averaging focuses on isolating flow features within a defined sector near the lower wall, and the coordinate representations previously introduced (see Fig. 8) can be performed to transform the original flow field to a rectangular domain. For such a simple configuration, the coarser mesh can be used to filter some flow variables by interpolation, so as to extract some critical information from the background turbulence. For example, the dataset of all spatial grid points in a single sector is defined as $\{\mathbf{r} = (\xi, \eta, \theta)|\xi \in [\xi_{\min}, \xi_{\max}], \eta \in [r_{\min}, r_{\max}], \theta \in [\theta_{\min}, \theta_{\max}]\}$, and each element can be mapped to the dataset of points in a cuboid $\{\mathbf{x} = (x_k, y_k, z_k)|x_k \in [x_{\min}, x_{\max}], y_k \in [y_{\min}, y_{\max}], z_k \in [z_{\min}, z_{\max}]\}$ one by one. Here, (x_k, y_k, z_k) can be flexibly used as any form of aforementioned coordinate representations, such as (x, y, z), (x_1, y_1, z_1), and (x_2, y_2, z_2). Consequently, the original data of BP can be interpolated to a new domain with sufficiently larger grid spacings and visualize the flow field to gain more understanding of the large-scale flow structures.

Figure 20 displays the three-dimensional view of isosurfaces of the streamwise vorticity in the BP after conditional averaging on the flow field within $\{(x_2, y_2, z_2)|x_2/\delta_i \in [-3, 15], y_2/\delta_i \in [0, 1.5], z_2/\delta_i \in [-6, 6]\}$. The streamwise vorticity marked in red (positive value) and blue (negative value) become apparent from $x_2/\delta_i > 0$.

The observation shows that the clockwise rotating vortices and anticlockwise rotating vortices alternate with each other in the circumferential distribution, suggesting the presence of the streamwise counterrotating vortical structures. Due to secondary flows, the difference in vorticity between the two sides is much greater than that in the central region. When focusing on the region boxed by the yellow dashed lines, it is found that these streamwise vortical structures appear parallel to each other in the case of small azimuthal angles. The dimensional wavelength λ is measured by the distance between two streamwise vortices in the same rotating direction, as labeled in the enlarged subfigure.

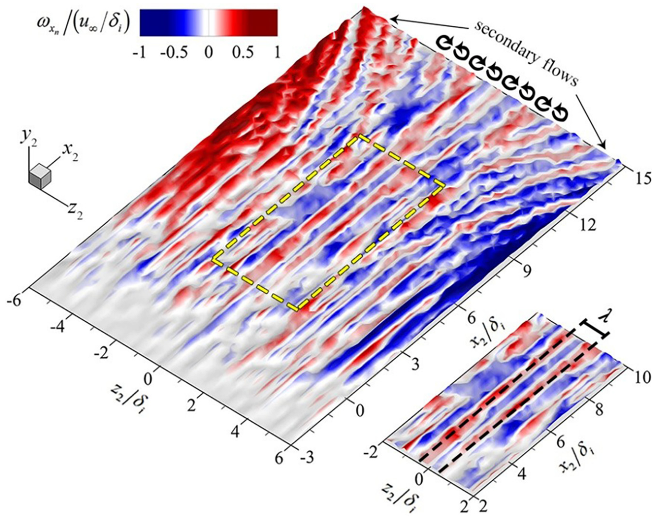

FIG. 20. Three-dimensional view of isosurfaces of the streamwise vorticity $\omega_{x_n}/(u_\infty/\delta_i)$ in the BP after conditional averaging, with an enlarged view of the region enclosed by the yellow dashed box. The red color represents clockwise rotation and the blue color represents anticlockwise rotation.

It proves that λ is slightly larger than the boundary thickness δ_i. For linear instability analysis, the dimensionless wavelength is defined as $\Lambda = \mathrm{Re}_\lambda\sqrt{\lambda/R^*}$, where Re_λ denotes the Reynolds number based on the wavelength λ. In addition, the dimensionless wave number is $\beta = 2\pi\theta^*/\lambda$, and the dimensionless growth rate is $\sigma = \beta\theta^{*2}/\nu_e^* = \beta\theta^*\mathrm{Re}_\theta^*$. The relationship between the Görtler number and the wave number is expressed as $G_T = \Lambda(\beta/2\pi)^{3/2}$ [55].

Figure 21 presents the results of the streamwise distribution of the local Görtler number in the lower boundary layer of the BP. The local Görtler number experiences a sustainable growth from the beginning of the bend, reaching a peak value of 4.74 at $x_2/\delta_i = 13.9$. Beyond the peak, it decreases rapidly. The processes of rising and falling are probably related to the APG and FPG, respectively. Furthermore, in the region of $2 \leqslant x_2/\delta_i \leqslant 10$ associated with the critical area identified in Fig. 20, the data from five positions with equal intervals are extracted to construct the (G_T, β, σ)

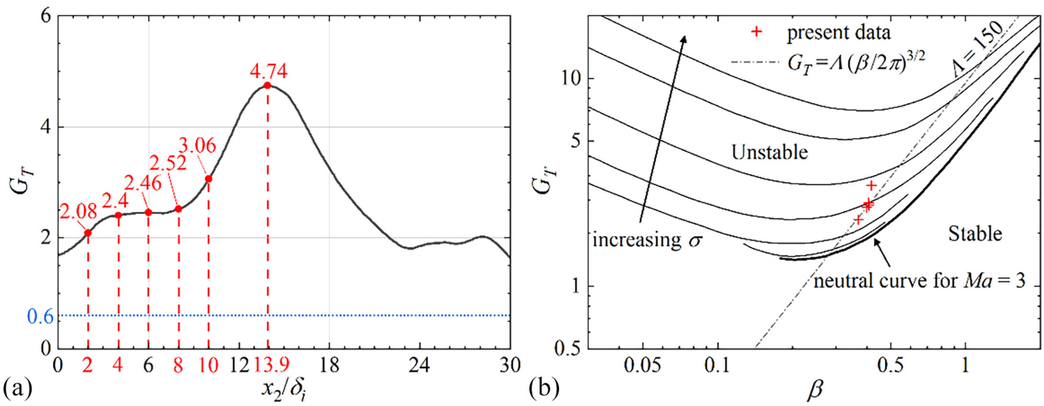

FIG. 21. (a) Streamwise distribution of the Görtler number in the lower boundary layer of the BP with the critical threshold of 0.6 [101], and (b) (G_T, β, σ) diagram for linear instability analysis, with the neutral curve and contours with constant growth rates cited from El-Hady and Verma [50].

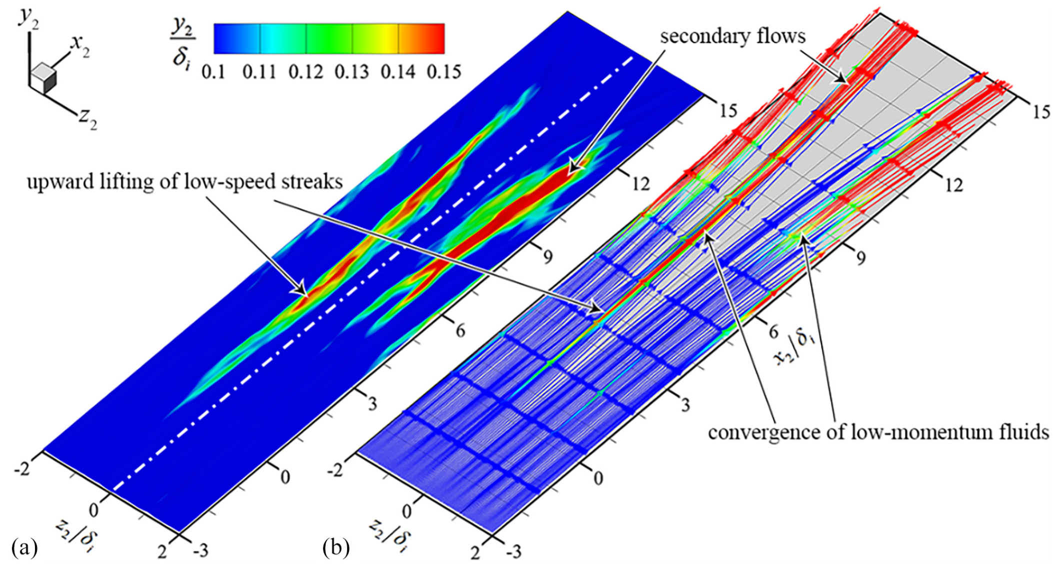

FIG. 22. Three-dimensional view of (a) isosurfaces of $\widetilde{u}/u_\infty = 0.5$ and (b) streamlines originating at $[x_2/\delta_i = -3, y_2/\delta_i = 0.1]$ in BP after conditional averaging, colored by the wall-normal distance y_2/δ_i.

diagram [Fig. 21(b)] for linear instability analysis, as marked in Fig. 21(a). In consideration of compressibility, the neutral curve and contours with constant growth rates are adopted under the condition of Ma $= 3$ [50]. The results demonstrate that the present data all fall above the neutral curve and generally align with the expected growth trend with a slope of $\frac{3}{2}$. Although the absolute growth rates remain relatively small, this quantitative evidence of linear instability supports the existence of the Görtler instability.

To investigate the response of the boundary layer to the increasing Görtler instability, the conditional averaging is performed in the flow field within $\{(x_2, y_2, z_2)|x_2/\delta_i \in [-3, 15], y_2/\delta_i \in [0, 1.5], z_2/\delta_i \in [-2, 2]\}$. Figure 22 provides a visualization of the low-speed isosurfaces and streamlines, which originate from uniformly distributed points at the identical x_2 and y_2 coordinates, revealing flow features and coherent structures that are otherwise concealed in the instantaneous flow field. Two prominent streaky structures are clearly visible on both sides of $z_2/\delta_i = 0$, covering the range of x_2/δ_i from 0 to 12. The streamlines suggest that increasing the Görtler instability leads to the clustering of low-momentum fluids, which are pumped away from the wall. When the Görtler instability begins to decline, the low-speed streaks descend and isosurfaces become smoother, whereas the upward-lifted fluids gradually merge into the high-speed flow. Furthermore, both the streak patterns and streamline trajectories indicate a secondary motion within the boundary layer, transporting the fluids from the lower to the upper side.

The slices of x_2/δ_i from -3 to 15 in intervals of 6 are extracted to trace the evolution of the streaks (see Fig. 23). Using a series of contours of $\widetilde{u}/u_\infty$, the spatial distribution of fluids with different velocities within the lower boundary layer is quantitatively visualized. The two streaks identified in Fig. 22 are located near $z_2/\delta_i = -0.6$ and $z_2/\delta_i = 1$, respectively. Under the influence of the Görtler instability, the wall-normal height of the low-speed contours exhibits an overall increase, with a greater wall-normal height corresponding to the higher fluid velocity. When the local Görtler number decreases, the boundary-layer fluid approaches the wall, contrasting with the behavior observed in the upstream straight section.

To evaluate the velocity fluctuations and turbulence intensity along the streamwise direction, Fig. 24 depicts the distribution of the Reynolds normal stress τ_{11}^+ at the aforementioned positions $z_2/\delta_i = -0.6$ and 1. As a key indicator of the turbulent intensity, the turbulent kinetic energy is

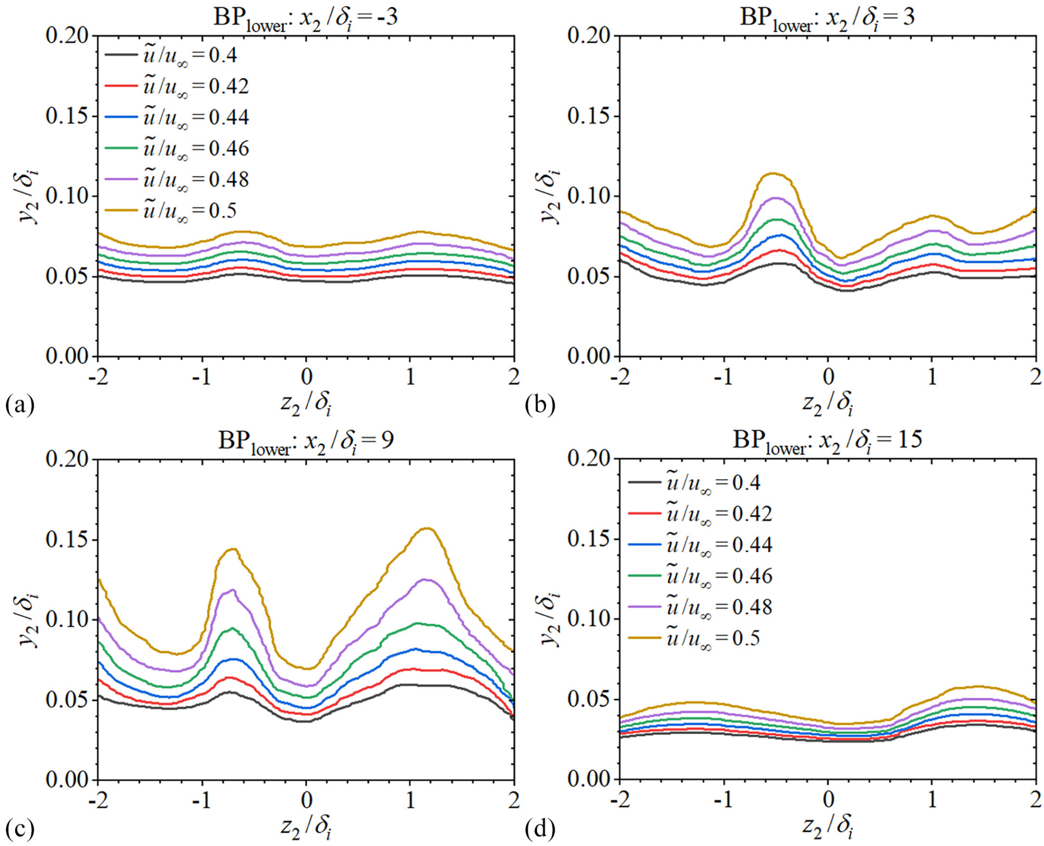

FIG. 23. Contours of $\tilde{u}/u_\infty$ (ranging from 0.4 to 0.5 in intervals of 0.02) at different streamwise positions in the BP after conditional averaging, including $x_2/\delta_i =$ (a) -3, (b) 3, (c) 9, and (d) 15.

calculated by $k^+ = \sum_{i=1}^{3} \tau_{ii}^+/2$. Although the finite duration of conditional averaging introduces certain variations in the distributions, it does not compromise the assessment of the influence of the Görtler instability. As the local Görtler number increases, the existing peak (inner peak, at $y^+ \approx 10$) moves closer to the wall, and the second peak emerges in the middle of the boundary layer (outer peak, at $y^+ \approx 100$). The occurrence of the outer peak indicates that the outer region of the turbulent boundary layer experiences stronger turbulence amplification than the inner region and also identifies the presence of the large-scale structure. This phenomenon suggests that the Görtler instability intensifies the Reynolds stresses and turbulent kinetic energy, which is consistent with the findings of Sun *et al.* [65] and Zhang *et al.* [102]. With a decrease in the Görtler instability, both peaks gradually diminish as the boundary-layer flow moves downstream.

Based on conditional averaging, the above investigation demonstrates the increasing Görtler instability within the APG region of lower boundary layer in the BP. However, the process of the Görtler number decreasing from its peak in the FPG region has not been discussed. To clarify the influence of the Görtler instability on the turbulent boundary layer, the following analysis focuses on three critical slices at $x_1/\delta_i = 0$, 11.3, and 22.6. These sections represent three distinct flow patterns: first, they correspond to the region dominated by the ZPG, APG, and FPG, respectively (see Figs. 11 and 12); second, on the lower wall of the BP, they typify a straight-pipe developing boundary layer, a thickening boundary layer, and a thinning boundary layer, respectively (see Figs. 17 and 18); and finally, they reflect the flow states before the rise, during the growth, and after the decline of

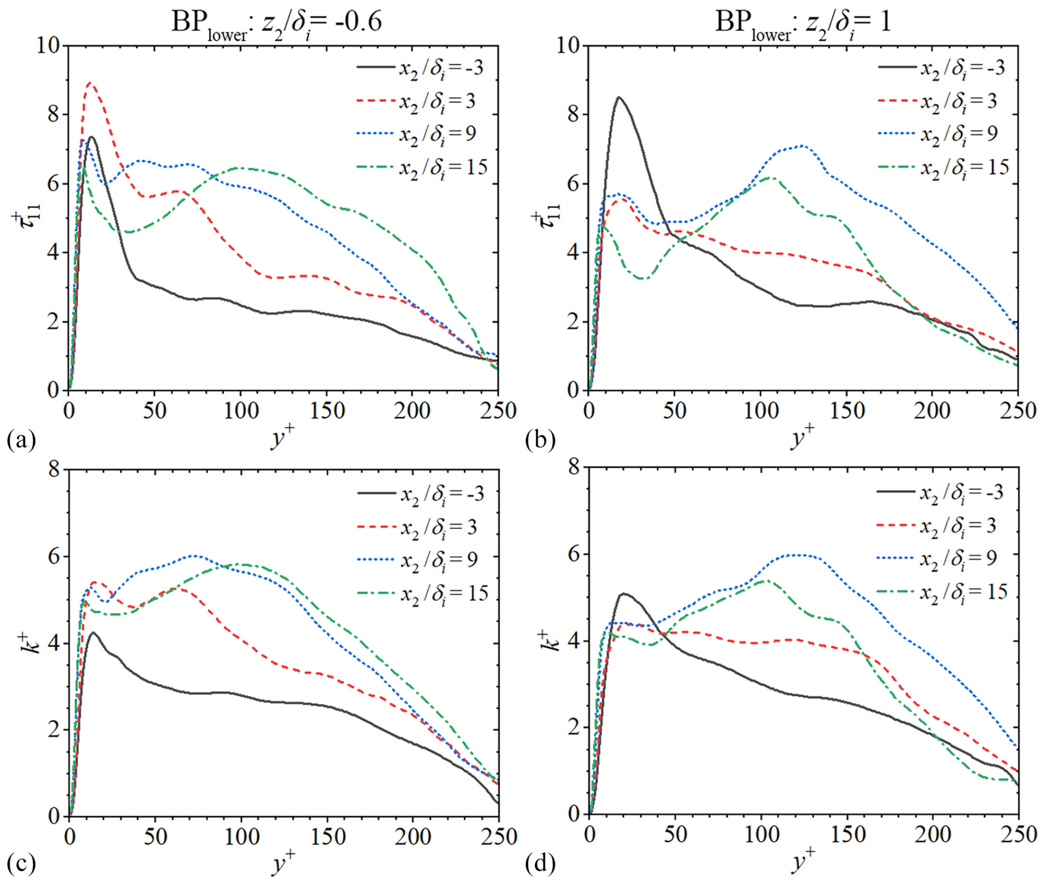

FIG. 24. Wall-normal distributions of (a), (b) the Reynolds normal stress τ_{11}^+ and (c), (d) the turbulent kinetic energy k^+ at (a), (c)$z_2/\delta_i = (-0.6$ and (b), (d) z_2/δ_i =1 in the BP after conditional averaging.

the Görtler number, respectively [see Fig. 21(a)]. The instantaneous velocity and vorticity fields are shown in Fig. 25. Recalling the discussion in Sec. III A, the extensive region of low velocity on the upper side at $x_1/\delta_i = 22.6$ results from the upstream separation. The vorticity is uniformly distributed around the circumferential wall at $x_1/\delta_i = 0$ and concentrated in the lower semicircular boundary layer at $x_1/\delta_i = 11.3$, and the vortex structures are significantly enriched in the low-speed turbulent region at $x_1/\delta_i = 22.6$. This phenomenon further demonstrates the substantial influence of the upper boundary-layer separation on the flow field in the BP. Streamlines in the central region indicate the fluid motion from the upper to the lower side, which is related to centrifugal effects of the mainstream flow. At $x_1/\delta_i = 11.3$, the streamlines in the lower boundary layer are dominated by the high Görtler instability. Moreover, compared with the other upstream positions, the slice at $x_1/\delta_i = 22.6$ displays a thinner turbulent boundary layer on the lower side, which is consistent with the previous discussion in Fig. 17.

To gain more comprehension of the vorticity field and quantitatively describe the influence of the Görtler instability, the vorticity transport equation governed in the compressible flows is written as

$$\frac{D\boldsymbol{\omega}}{Dt} = \underbrace{(\boldsymbol{\omega} \cdot \nabla)\mathbf{u}}_{\mathbf{S}} - \underbrace{\boldsymbol{\omega}(\nabla \cdot \mathbf{u})}_{\mathbf{D}} - \underbrace{\rho^{-2}(\nabla p \times \nabla \rho)}_{\mathbf{B}} + \underbrace{\nabla \times (\rho^{-1}\nabla \cdot \boldsymbol{\tau})}_{\boldsymbol{\varepsilon}}, \tag{9}$$

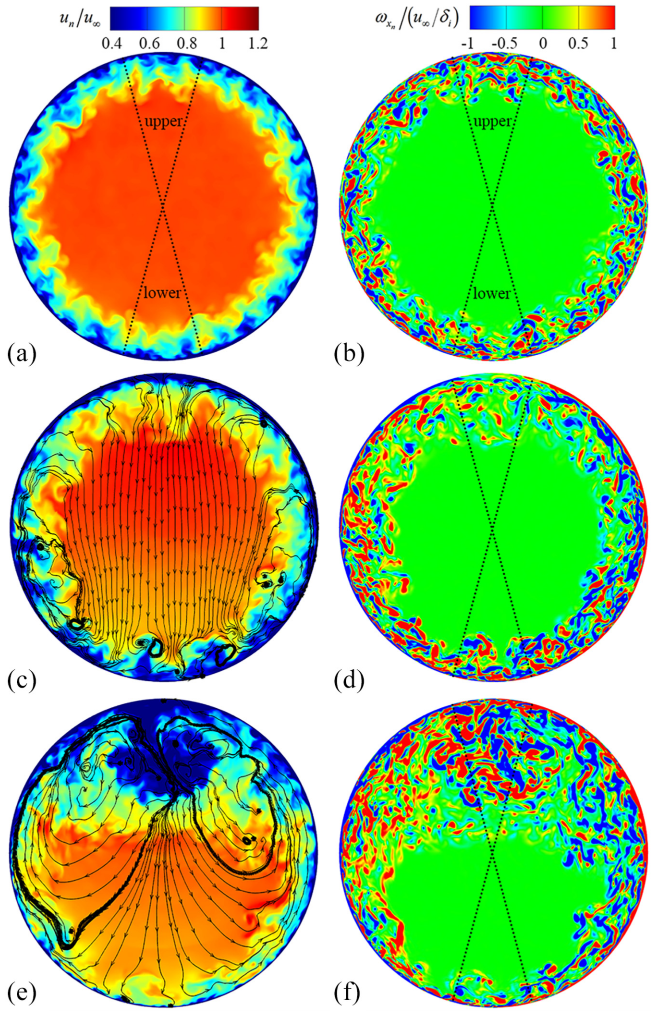

FIG. 25. Instantaneous (a), (c), (e) velocity fields u_n/u_∞ and (b), (d), (f) vorticity fields $\omega_{x_n}/(u_\infty/\delta_i)$ at different streamwise positions in the BP, including (a), (b) $x_1/\delta_i = 0$, (c), (d) $x_1/\delta_i =$11.3, and (e), (f) $x_1/\delta_i =$ 22.6. The black dotted lines in (a) and (b) represent the boundaries of the upper and lower sides for conditional spatial averaging. The black arrows in (c) and (e) denote the streamlines perpendicular to the primary flow direction.

where **S** denotes the vortex stretching term, **D** is the dilatational term, **B** is the baroclinic term, and $\boldsymbol{\varepsilon}$ is the diffusive term. The specific introduction of these terms can be found in the literatures on vortex flows (e.g., Ref. [103]). A quantitative analysis of the first three terms on the right-hand side of Eq. (9) is conducted to assess the influence of flow variables at different locations within the flow field (see Fig. 26). The dissipation effect of the Reynolds stresses is reflected in the following investigation of the Reynolds stresses and turbulent kinetic energy (see Fig. 27).

Although higher peaks of the vortex stretching term **S** and the dilatational term **D** emerge at the two downstream positions ($x_1/\delta_i = 11.3$ and 22.6) in the lower boundary layer of the BP than those at $x_1/\delta_i = 0$, their influence is limited to $y^+ < 20$. This phenomenon illustrates that the vorticity production is concentrated in the inner layer (near the wall), whereas the generation of vortices is weakened in the outer region (near the mainstream). Notably, the baroclinic term **B** at $x_1/\delta_i =$ 11.3 shows a distinct second peak [pointed by the black arrow in Fig. 26(c)], indicating a strong

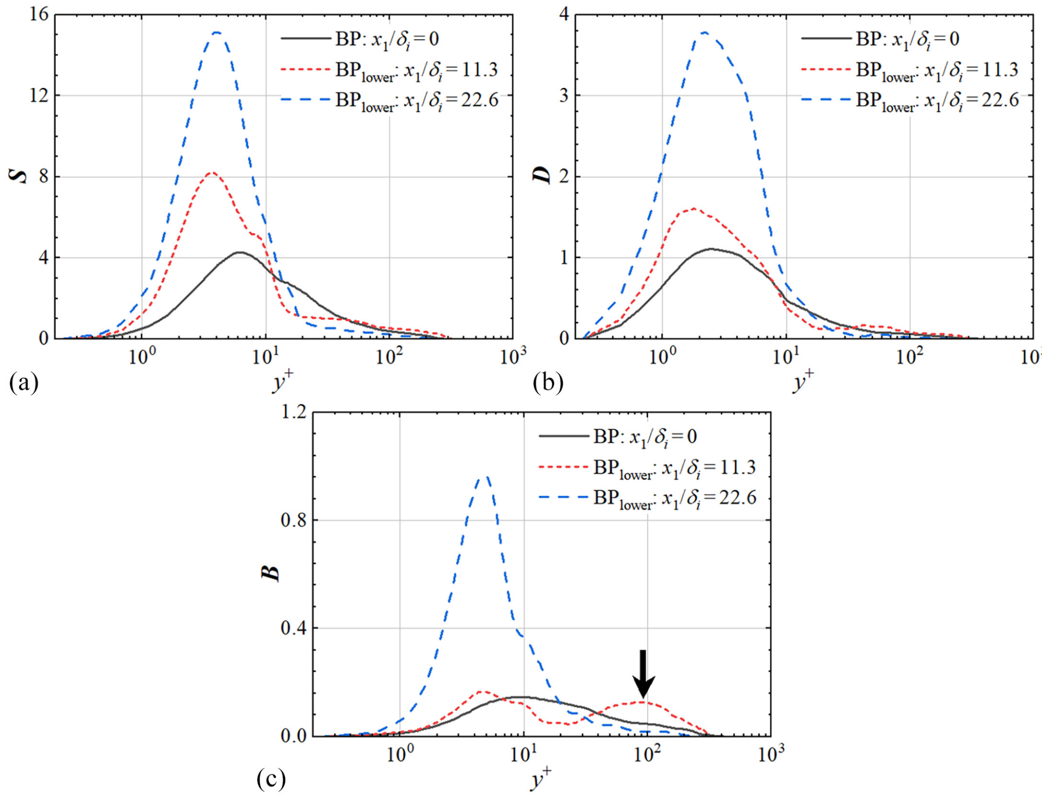

FIG. 26. Wall-normal distributions of the magnitude of (a) the vortex stretching term **S**, (b) the dilatational term **D**, and (c) the baroclinic term **B** in Eq. (9), normalized by $(u_\infty/\delta_i)^2$ at different positions, including $x/\delta_i = 0$ in the SP, $x_1/\delta_i = 0$, 11.3, and 22.6 in the BP. Here, the statistics of the BP are obtained in both the upper and lower regions.

orthogonality between the density and pressure gradients in the lower side, especially in the outer region where the boundary layer interacts with the free-stream flow. As explained by Sun *et al.* [65], the Görtler instability can twist local density gradients and cause a prominent baroclinic effect in the destabilized boundary layer, thus inducing the significant vorticity and promoting the formation of abundant small-scale vortices. Therefore, the increase of the Görtler instability positively contributes to the generation of vortices in the lower turbulent boundary layer.

Figure 27 illustrates the distribution of the Reynolds stresses and turbulent kinetic energy in the lower region of the BP at different streamwise locations. The inner peaks of the τ_{11}^+ at $x_1/\delta_i = 11.3$ and 22.6 are closer to the wall compared to that at the inlet, and an outer peak emerges near the mainstream. Both the τ_{22}^+ and τ_{33}^+ exhibit an overall increase in $x_1/\delta_i = 11.3$ compared with $x_1/\delta_i = 0$. Except for a peak occurring at $y^+ \approx 5$ on the curve of τ_{22}^+, the Reynolds stresses at $x_1/\delta_i = 22.6$ are smaller than those corresponding variables at $x_1/\delta_i = 11.3$. The turbulent kinetic energy k^+ at $x_1/\delta_i = 11.3$ has the highest inner peak value and a second peak at $y^+ \approx 100$, while the curve of k^+ at $x_1/\delta_i = 22.6$ is lower than the former but retains the second peak distinct from that at the inlet. This comparative analysis clearly reflects the variations of wall stresses and the turbulent intensity affected by the increase and decrease of the Görtler instability.

C. Responses of turbulence to curvature in bent pipes

The investigation on the response of turbulence to the curvature primarily focuses on the pressure gradient because it plays an essential role in stabilizing or destabilizing boundary layers and

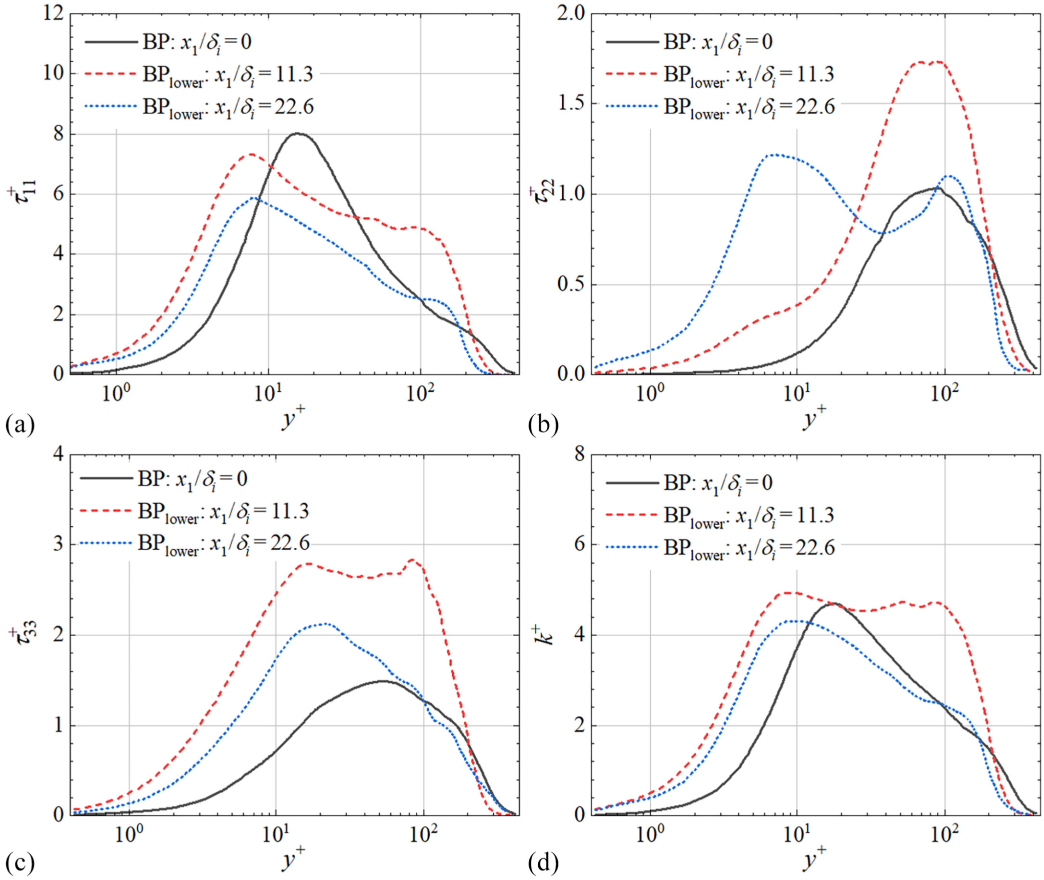

FIG. 27. Wall-normal distributions of the Reynolds stresses (a) τ_{11}^+, (b) τ_{22}^+, (c) τ_{33}^+, and (d) the turbulent kinetic energy k^+ at different positions, including $x_1/\delta_i = 0$, 11.3, and 22.6 on the lower region of the BP.

causing the growth or decay of turbulent intensity. The velocity field in the BP (Fig. 28) exhibits distinct features in the critical simulation region, suggesting that the boundary layer experiences intricate flow patterns at different azimuthal angles. To facilitate the illustration, the velocity field is divided into three distinct parts based on the morphological changes and moving patterns of the streaks. First, the streaks that move from the lower to the upper side indicate the presence of secondary flows (Dean vortices), which can promote the transport of mass, heat, and momentum within the boundary layer. Second, the continuous streaks on the upper side are disrupted by a low-speed region, suggesting that the boundary-layer flow is separated at the front and then reattached at the back. As in the aforementioned analysis, the decrease in the fluid velocity due to the convex curvature, in conjunction with the APG conditions due to the shock-wave–boundary-layer interaction, resulted in separation. Third, in the lower region within $-\pi/4 \lesssim \theta \lesssim \pi/4$, the streaks gradually disperse when moving across $0 < x_2/\delta_i \lesssim 14$ and rapidly cluster beyond $x_2/\delta_i \gtrsim 14$. Meanwhile, the boundary-layer flow on the lower side sequentially traverses the ZPG-APG-FPG region, as depicted in Fig. 11(d). In addition to the impact of pressure gradients, the boundary layer on the concave wall is significantly affected by the Görtler instability, which is comprehensively discussed in Sec. III B.

To provide an overview of the supersonic boundary layers in pipes, Fig. 29 depicts the isosurfaces of λ_2 to visualize the vortex structures within boundary layers of the SP and BP. The original form of

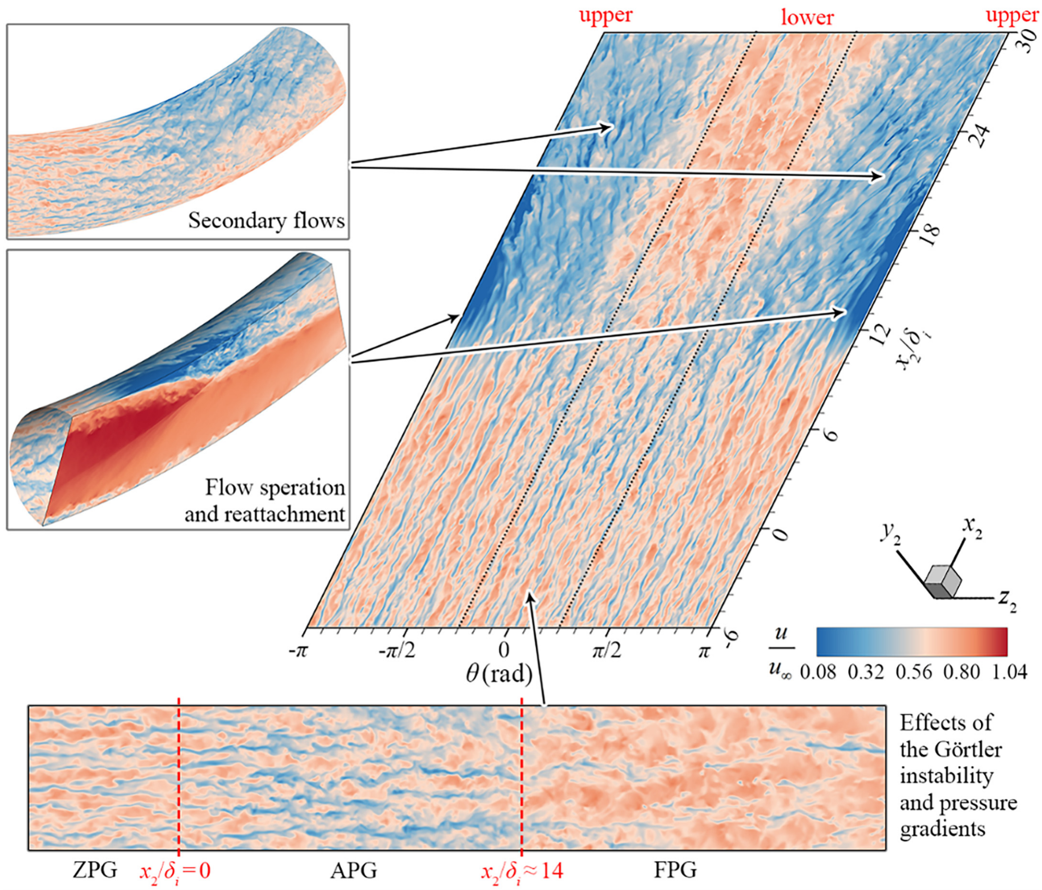

FIG. 28. Instantaneous velocity field u/u_∞ on the isosurface of $y^+ = 30$ in the BP. The arrows identify the following phenomena: streaks moving from the lower to the upper side due to secondary flows, the backflow in the upper region indicating separation and reattachment, and the dispersing and clustering of streaks implying the lower boundary layer changes under the combined influence of the local Görtler instability and pressure gradients.

the boundary layer in a bent pipe is shown in Fig. 6 and the coordinate transformation "unfolding" is illustrated by Eq. (6). Notably, the aforementioned division of regions in Fig. 16 is performed to explore the characteristics and underlying mechanisms of each region as follows. Notably, the boundary layer without the influence of compression or expansion (the region I) maintains the characteristics of the straight pipe section. The generation of new vortices and the enhancement of the turbulent intensity in the region II are likely related to the effect of the Görtler instability, which is also the typical response of the boundary layer to the concave curvature. In supersonic flows, compression waves on the concave surface often induce large pressure fluctuations across the boundary layer, which breaks the balance between the centrifugal force and wall-normal pressure gradients and causes centrifugal instability. Consequently, the region II may show the baroclinic effect of the Görtler instability, which are linked to the newly generated small-scale vortices. Region III includes the effects of expansion and separation on the upper side of the BP. The existing vortices become rarer than those in the ZPG region before the separation point, while a sudden proliferation of vortices with low speeds and high energies is observed upon flow separation. The upper boundary layer downstream of the reattachment point is filled with low-speed fluids and abundant vortex

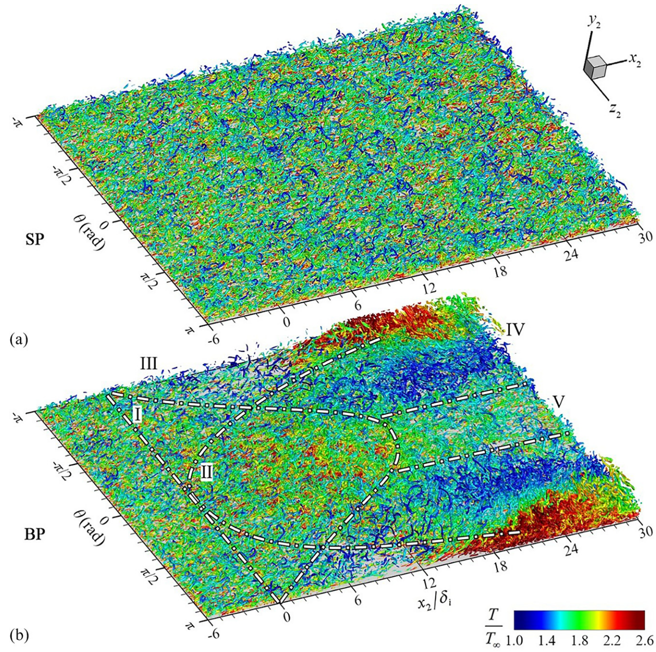

FIG. 29. Instantaneous isosurfaces of $\lambda_2 = -2 \times 10^4$ in the (a) SP and (b) BP, colored by the temperature T/T_∞. The region $y_2/\delta_i > 2$ is excluded to clearly visualize the vortex field. The white dotted-dashed line denotes the approximate boundaries of regions I–V within the boundary layer of the BP.

structures. In the region IV, the vortices within the boundary layer are enriched because of the interactions with compression waves, and the cooling effects caused by the expansion waves can also be observed. Recalling the analysis in Fig. 12, as the dominant advantage of compression waves in the lower boundary layer is occupied by expansion waves downstream, the region V witnesses a shift from the APG to FPG, which is the reason of the reduction in turbulence.

The velocity fluctuations of the supersonic flow field in the BP are analyzed below, focusing on $\langle uu\rangle^+$ and $\langle vv\rangle^+$ to highlight the prominent regions on both the upper and lower sides, as shown in Fig. 30. $\langle uu\rangle^+$ represents the normal stress component, which is particularly important for the momentum and energy transport within the boundary layer, and $\langle vv\rangle^+$ also makes great contribution to the turbulent kinetic energy in bent pipes [104]. In Fig. 30(a), the interaction between shock waves and boundary layers gives rise to high velocity fluctuations. In addition, the turbulent boundary layer separation seems to be the primary factor contributing to the increase in normal stress before the point of the shock-wave–boundary-layer interaction in the upper region of the BP. The prominent bandlike region clearly identifies the shear layer at the interface between the separated turbulent boundary layer (or the low-speed turbulent region) and the mainstream, which serves as the transition zone between the low-speed and the high-speed flows. Furthermore, these regions of notable velocity fluctuations coincide with the APG regions in the BP, suggesting that the APG substantially contributes to the enhancement of the Reynolds stresses, as explained by Neel *et al.* [43].

To evaluate the impact of separation on the turbulence statistics, the positions $x_1/\delta_i = 20.3$ and 2.4 are chosen to make comparisons with the Reynolds stresses and turbulent intensity, as shown in Fig. 31. The observations show that compared with the Reynolds stresses at the inlet, those at $x_1/\delta_i = 2.4$ are enhanced in all directions, thus causing an increase in the turbulent kinetic energy in the lower boundary layer. However, the amplification of the turbulent intensity at $x_1/\delta_i = 20.3$ in the upper region appears to be significantly stronger. Although the τ_{11}^+ of the curve of $x_1/\delta_i = 20.3$

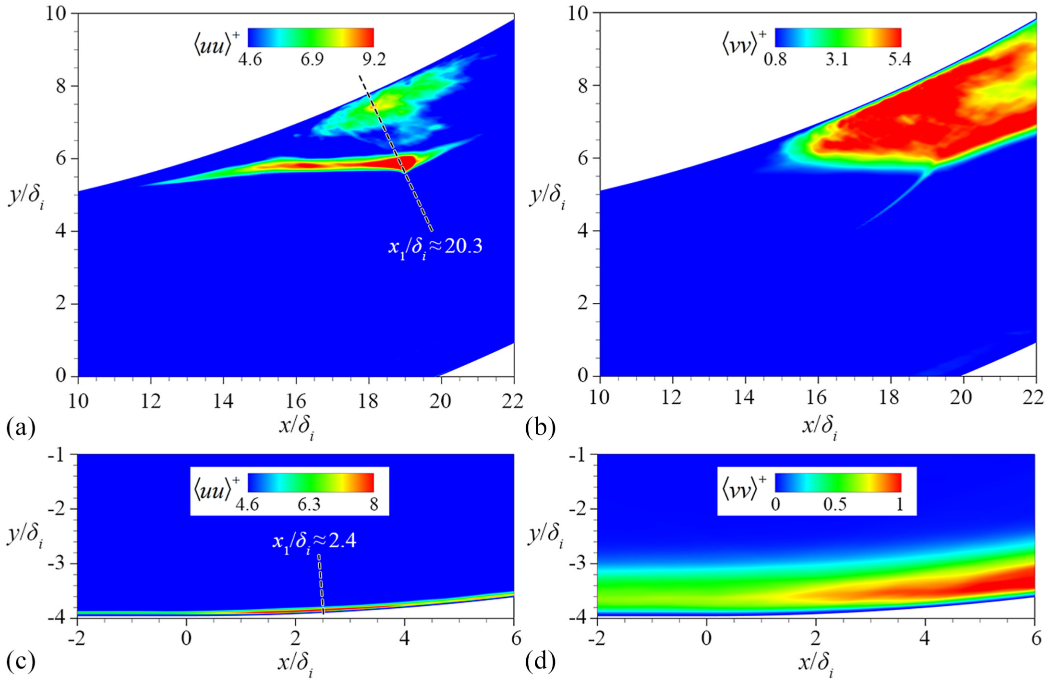

FIG. 30. Contours of velocity fluctuations (a), (c) $\langle uu \rangle^+$ and (b), (d) $\langle vv \rangle^+$ in the regions of (a), (b) $(10 < x/\delta_i < 22, 0 < y/\delta_i < 10)$ and (c), (d) $(-2 < x/\delta_i < 6, -4 < y/\delta_i < -1)$ on the x-y plane in the BP.

is slightly smaller near the wall compared to the inlet, the data of τ_{22}^+ and τ_{33}^+ on the upper side comprehensively exceed those on the lower side. It is because the confined internal geometry of the BP, the compression shock wave originating from the outer wall can not only increase the lower boundary-layer instability, but also propagate downstream and interact with the upper boundary layer. Therefore, the physical mechanisms of turbulence enhancement on the upper and lower sides of the BP are fundamentally distinct. The results illustrate that the flow separation in the upper boundary layer exerts a stronger contribution on turbulence than the APG effect in the lower boundary layer. As stated by Simpson [95], the turbulent boundary layer separation corresponds to a sudden thickening of the rotational flow region near the wall, accompanied by substantial Reynolds stresses that are as large as the mean velocity in the backflow; otherwise, this region would not have any significant interaction with the free-stream flow. This observation confirms that the turbulence is intensified under the influence of separated flows, as opposed to the boundary-layer regions where separation is not present. Additionally, a secondary peak of k^+ is found at $y^+ \approx 500$, which is the point of shock impact with the upper boundary layer, indicating that the shock-wave–boundary-layer interaction is also one of the most important sources of turbulent kinetic energy.

The amplification effect of turbulence on the concave surface is delineated by Wang *et al.* [66] using the quadrant decomposition. It was proposed by Lu and Willmarth [105] and has been widely applied to study turbulent boundary-layer events [106,107]. The Reynolds shear stress component on the lower boundary layer of the BP can be divided into different turbulence events, which are quantified from the fluctuation statistics in the conditional lower region (see Fig. 25). The correlation between u' and v' (or w') reveals the presence of turbulent coherent structures, where the four quadrants $i = 1, 2, 3,$ and 4 characterize the following types of burst events: outward interactions Q1, $u' > 0$, $v' > 0$ (or $w' > 0$); ejections Q2, $u' < 0$, $v' > 0$ (or $w' > 0$); inward interactions Q3, $u' < 0$, $v' < 0$ (or $w' < 0$); and sweeps Q4, $u' > 0$, $v' < 0$ (or $w' < 0$).

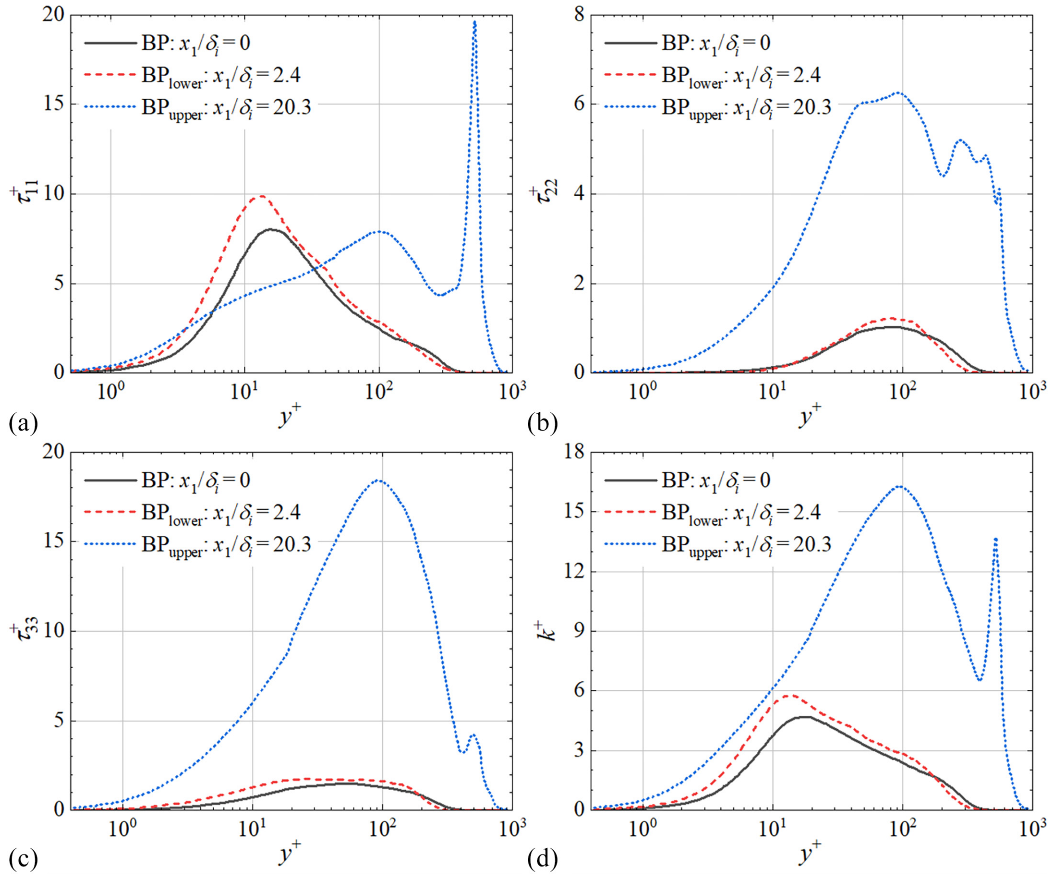

FIG. 31. Wall-normal distributions of the Reynolds stresses (a) τ_{11}^{+}, (b) τ_{22}^{+}, (c) τ_{33}^{+}, and (d) the turbulent kinetic energy k^+ at different streamwise positions, including $x_1/\delta_i = 0$, $x_1/\delta_i = 2.4$ on the lower side and $x_1/\delta_i = 20.3$ on the upper side of the BP.

The scatter plots extracted in the conditional lower region at three critical streamwise positions $x_1/\delta_i = 0$, 11.3, and 22.6 are shown in Fig. 32. At $x_1/\delta_i = 11.3$ and 22.6, the probability of positive or negative velocity fluctuations increases significantly, with u' exceeding $0.3u_\infty$, v' exceeding $0.1u_\infty$, and w' exceeding $0.15u_\infty$ compared to that at the inlet. Typically, the increase at $x_1/\delta_i = 11.3$ is more pronounced than that at $x_1/\delta_i = 22.6$. The scatter plots in Figs. 32(a) and 32(b) show an uneven distribution across the four quadrants, with larger ranges for Q2 and Q4 and smaller ranges for Q1 and Q3. Figure 32(c) exhibits larger ranges for Q1, Q2, and Q3, but a smaller range for Q4. However, the scatter points in Figs. 32(d)–32(f) appear to be evenly distributed across the four quadrants, showing a symmetrical distribution. In summary, these observations indicate that the turbulence characteristics at $x_1/\delta_i = 11.3$ and 22.6 are more pronounced than at the inlet, with $x_1/\delta_i = 11.3$ exhibiting strongest turbulence activity.

To further investigate the respective contributions of different events, scatter data are statistically analyzed to evaluate the proportion of each quadrant. According to Tichenor *et al.* [107] and Wang *et al.* [66], taking $u'v'$ for example, the conditional average result for each quadrant can be calculated by

$$\sum_{n=1}^{N_i} (u'v')/N_i = \overline{(u'v')}_i \triangleq \langle uv \rangle_i, \tag{10}$$

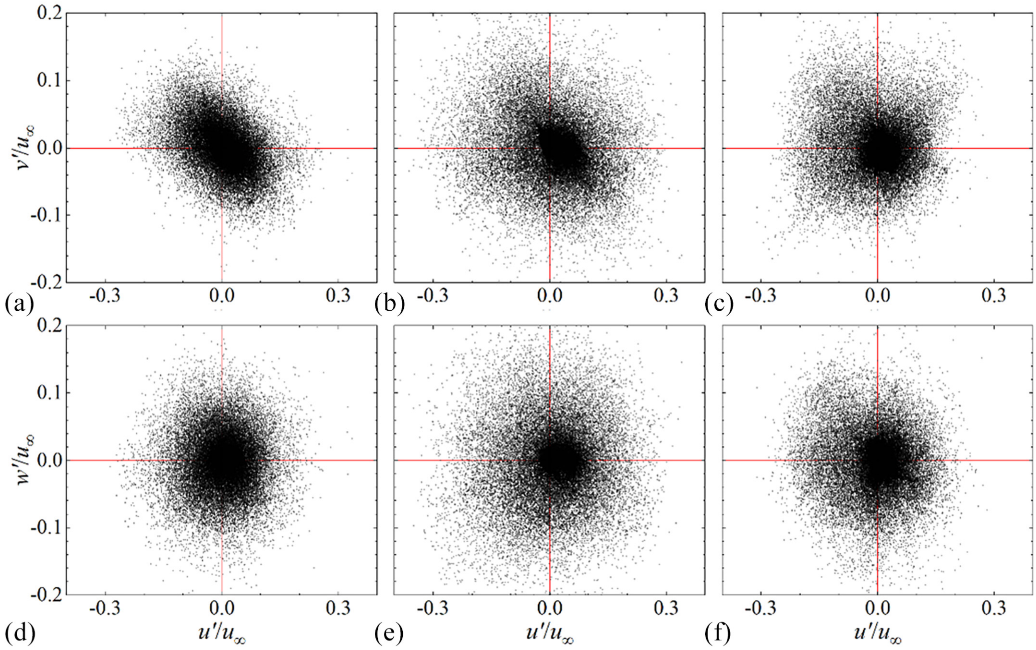

FIG. 32. Scatter plots of the velocity fluctuations and quadrant decompositions for (a)–(c) $u'v'$ and (d)–(f) $u'w'$ normalized by the free-stream velocity u_∞ at different positions within the conditional lower region of the BP, including (a), (d) $x_1/\delta_i = 0$, (b), (e) x_1/δ_i =11.3, and (c), (f) x_1/δ_i =22.6.

and the global average result is defined as

$$\sum_{n=1}^{N}(u'v')/N = \overline{u'v'} \triangleq \langle uv \rangle, \tag{11}$$

where N_i denotes the sample number for the ith quadrant, and N is the total number of samples. This process can similarly be applied to $u'w'$.

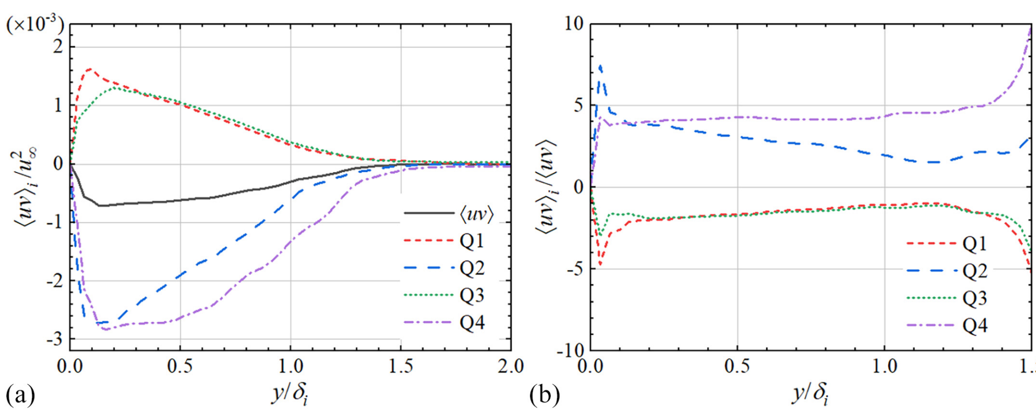

FIG. 33. Profiles of the quadrant-decomposed components $\langle uv\rangle_i$ scaled by (a) u_∞^2 and (b) the global average $\langle uv \rangle$ at the streamwise position of $x_1/\delta_i = 0$ within the conditional lower region of the BP.

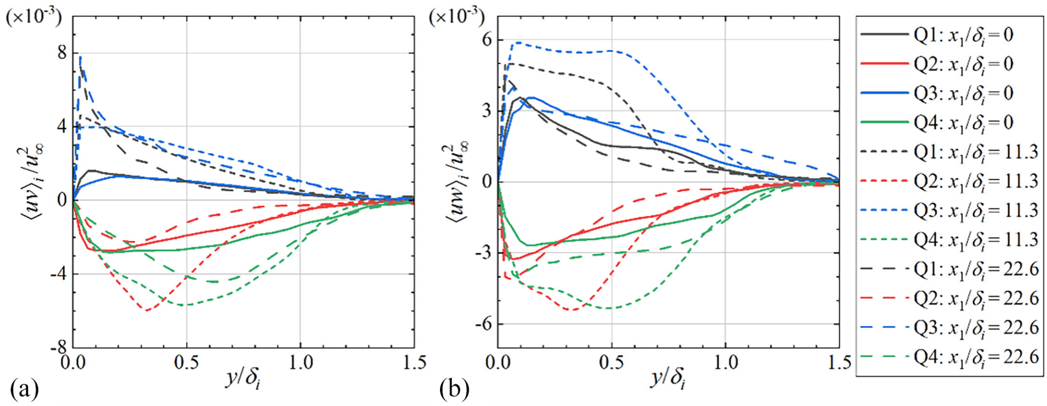

FIG. 34. Profiles of the quadrant-decomposed components (a) $\langle uv\rangle_i$ and (b) $\langle uw\rangle_i$ scaled by u_∞^2 at different streamwise positions within the conditional lower region of BP, including $x_1/\delta_i = 0$, 11.3, and 22.6.

The profiles of the average results $\langle uv\rangle_i$ for the four quadrants at $x_1/\delta_i = 0$ are shown in Fig. 33. For the four quadrants of the turbulent boundary layer, the curves almost peaked at the wall-normal position of $y/\delta_i \approx 0.1$. The negative values of the Q2 and Q4 events are much larger than those of the Q1 and Q3 events. In the inner region, the Q2 event contributes the most to the $\overline{u'v'}$. However, with an increasing wall-normal distance for $y/\delta_i > 0.1$, the Q2 curve decreases gradually, and the Q4 event dominates $\overline{u'v'}$. These findings at the inlet of the BP are consistent with the results for the flat-plate case [66].

By comparing the quadrant decomposition of $u'v'$ at different positions, $x_1/\delta_i = 0$, 11.3, and 22.6, as shown in Fig. 34(a), the influence of the Görtler instability on the turbulence events can be revealed. As the flow transverses the bend, the peaks of Q1 and Q3 at $y/\delta_i \approx 0.1$ continue to increase, and the peak positions of Q2 and Q4 tend to move outward from the wall. With the rising Görtler number and the influence of APG, the absolute value of $\langle uv\rangle_i$ is strengthened within $0.3 \lesssim y/\delta_i \lesssim 1$ for all quadrants. In contrast, the absolute value of $\langle uv\rangle_i$ at $x_1/\delta_i = 22.6$ is lower than that at $x_1/\delta_i = 11.3$. In summary, the increase of the Görtler instability specifically enhances the ejections and sweeps. Additionally, the probability of the Q4 event at $x_1/\delta_i = 22.6$ is lower than that at $x_1/\delta_i = 0$; this implies that the falling of the Görtler instability or the effect of FPG restrains the sweeps in the lower boundary layer of the BP.

The quadrant decomposition of $u'w'$ [see Fig. 34(b)] shows that Q1 and Q2, as well as Q3 and Q4, are mirror symmetric about the horizontal line of the theoretical probability $\overline{u'w'} = 0$. This finding agrees with the opinion of Barlow and Johnston [44] that the boundary layer in the pipe bend lacks spanwise inhomogeneity. With the increasing Görtler instability, the absolute value of $\langle uw\rangle_i$ is greatly amplified for all quadrants. As the Görtler instability dissipates downstream, the absolute value of $\langle uw\rangle_i$ returns to the original level at the inlet or even lower. In conclusion, the increase or decrease of the Görtler instability does not exclusively enhance or decay any of the quadrant-decomposed components.

IV. CONCLUSIONS

This study used DNS to explore the supersonic bent-pipe flow at a Mach number of 3.0 and a Dean number of 824. The flow is more complex than that in straight pipe owing to the interplay of multiple competing mechanisms, including convex and concave curvatures, APG and FPG, and compression and expansion waves. The compressibility of the supersonic flow also has a significant influence on the velocity, density, and temperature profiles of boundary layers in the bent pipe. An effective coordinate transformation is proposed to visualize both instantaneous and time-averaged flow fields in the bent pipe. The high pressure caused by the downstream shock-wave–boundary-layer interaction induces the APG, and the measurement of the skin friction coefficient confirms that separation occurs in the upper boundary layer. Furthermore, consistent with incompressible flows, Dean vortices are also visualized in the circumferential boundary layer of the bent pipe.

An increasing Görtler number and the linear instability analysis suggest that the Görtler instability is enhanced in the APG region of the lower boundary layer. Conditional averaging indicates the formation of large-scale streamwise vortices in this region, where low-speed streaks are lifted up from the wall, contributing to the destabilization of the boundary layer. The investigation of vorticity transport terms suggests that the Görtler instability causes significant baroclinic effects, thereby enhancing the Reynolds stresses and turbulent intensity near the mainstream. Since the pressure gradient has a great impact on the Görtler instability in the turbulent boundary layer, the Görtler instability decreases and the turbulence decays in the downstream FPG region. Nevertheless, a second peak in the wall-normal distribution of turbulent kinetic energy persists in the outer region of the boundary layer.

The response of turbulence to the curvature is primarily governed by pressure gradients within boundary layers in the bent pipe. The combined effects of the APG and convex curvature contribute to boundary-layer separation, inducing a thickening low-speed turbulent region and significantly amplified velocity fluctuations and turbulent intensity. Under the influence of compression and expansion waves, the lower region exhibits a ZPG-APG-FPG distribution along the streamwise direction, while the upper region follows a ZPG-FPG-APG distribution. The pressure gradient plays an important role in the spatial organization of small-scale vortices. The quadrant decomposition analysis conducted in the lower region shows that the rising Görtler number and the effect of the APG are related to the amplification of ejections (Q2; $u' < 0$, $v' > 0$) and sweeps (Q4; $u' > 0$, $v' < 0$), whereas the falling Görtler number and the influence of the FPG specifically make a negative contribution to sweeps (Q4; $u' > 0$, $v' < 0$). The increase or decrease of the Görtler instability does not individually strengthen or weaken any turbulence event of $u'w'$.

The findings of this study advance the understanding of the flow characteristics and turbulence structures of supersonic boundary layers in bent pipes. To further explore and validate bent-pipe flows, future studies should be focused on the three-dimensional effects of shock-wave–boundary-layer interactions, curvature and Mach number effects of the supersonic bent pipes, responses of turbulence to different frequencies and curvatures, and experimental verification of Görtler-type vortices in turbulent boundary layers. This study can provide theoretical support for the optimal design of air-intake systems for air-breathing hypersonic vehicles.

ACKNOWLEDGMENT

This work was supported by the National Natural Science Foundation of China (Grants No. 12525202 and No. T2221002).

The authors report no conflict of interest.

DATA AVAILABILITY

There are no publicly available research data or software supporting this manuscript. Requests for further information or data should be sent to the authors.

[1] S. E. Guarini, R. D. Moser, K. Shariff, and A. Wray, Direct numerical simulation of a supersonic turbulent boundary layer at Mach 2.5, J. Fluid Mech. **414**, 1 (2000).

[2] T. Maeder, N. A. Adams, and L. Kleiser, Direct simulation of turbulent supersonic boundary layers by an extended temporal approach, J. Fluid Mech. **429**, 187 (2001).

[3] S. Pirozzoli, F. Grasso, and T. B. Gatski, Direct numerical simulation and analysis of a spatially evolving supersonic turbulent boundary layer at $M = 2.25$, Phys. Fluids **16**, 530 (2004).
[4] M. Bernardini and S. Pirozzoli, Wall pressure fluctuations beneath supersonic turbulent boundary layers, Phys. Fluids **23**, 085102 (2011).
[5] A. Di Marco, R. Camussi, M. Bernardini, and S. Pirozzoli, Wall pressure coherence in supersonic turbulent boundary layers, J. Fluid Mech. **732**, 445 (2013).
[6] H. Foysi, S. Sarkar, and R. Friedrich, Compressibility effects and turbulence scalings in supersonic channel flow, J. Fluid Mech. **509**, 207 (2004).
[7] S. Ghosh, H. Foysi, and R. Friedrich, Compressible turbulent channel and pipe flow: Similarities and differences, J. Fluid Mech. **648**, 155 (2010).
[8] D. Modesti and S. Pirozzoli, Reynolds and Mach number effects in compressible turbulent channel flow, Int. J. Heat Fluid Flow **59**, 33 (2016).
[9] M. Yu, C. X. Xu, and S. Pirozzoli, Compressibility effects on pressure fluctuation in compressible turbulent channel flows, Phys. Rev. Fluids **5**, 113401 (2020).
[10] A. Baranwal, D. A. Donzis, and R. D. W. Bowersox, Asymptotic behaviour at the wall in compressible turbulent channels, J. Fluid Mech. **933**, A28 (2022).
[11] S. Pirozzoli, J. Romero, M. Fatica, R. Verzicco, and P. Orlandi, One-point statistics for turbulent pipe flow up to $\mathrm{Re}_\tau \approx 6000$, J. Fluid Mech. **926**, A28 (2021).
[12] J. G. M. Eggels, F. Unger, M. H. Weiss, J. Westerweel, R. J. Adrian, R. Friedrich, and F. T. M. Nieuwstadt, Fully developed turbulent pipe flow: A comparison between direct numerical simulation and experiment, J. Fluid Mech. **268**, 175 (1994).
[13] N. Afzal, Power law and log law velocity profiles in fully developed turbulent pipe flow: Equivalent relations at large Reynolds numbers, Acta Mech. **151**, 171 (2001).
[14] J. P. Monty, J. A. Stewart, R. C. Williams, and M. S. Chong, Large-scale features in turbulent pipe and channel flows, J. Fluid Mech. **589**, 147 (2007).
[15] G. K. El Khoury, P. Schlatter, A. Noorani, P. F. Fischer, G. Brethouwer, and A. V. Johansson, Direct numerical simulation of turbulent pipe flow at moderately high Reynolds numbers, Flow Turbul. Combust. **91**, 475 (2013).
[16] D. Modesti and S. Pirozzoli, Direct numerical simulation of supersonic pipe flow at moderate Reynolds number, Int. J. Heat Fluid Flow **76**, 100 (2019).
[17] P. H. M. Bovendeerd, A. A. V. Steenhoven, F. N. V. D. Vosse, and G. Vossers, Steady entry flow in a curved pipe, J. Fluid Mech. **177**, 233 (1987).
[18] Y. Fan, R. I. Tanner, and N. Phan-Thien, Fully developed viscous and viscoelastic flows in curved pipes, J. Fluid Mech. **440**, 327 (2001).
[19] P. L. Wilson and F. T. Smith, The development of the turbulent flow in a bent pipe, J. Fluid Mech. **578**, 467 (2007).
[20] J. Sakakibara and N. Machida, Measurement of turbulent flow upstream and downstream of a circular pipe bend, Phys. Fluids **24**, 041702 (2012).
[21] C. Carlsson, E. Alenius, and L. Fuchs, Swirl switching in turbulent flow through 90° pipe bends, Phys. Fluids **27**, 085112 (2015).
[22] L. Hufnagel, J. Canton, R. Örlü, O. Marin, E. Merzari, and P. Schlatter, The three-dimensional structure of swirl-switching in bent pipe flow, J. Fluid Mech. **835**, 86 (2018).
[23] S. Vashisth, V. Kumar, and K. D. P. Nigam, A review on the potential applications of curved geometries in process industry, Ind. Eng. Chem. Res. **47**, 3291 (2008).
[24] A. K. Vester, R. Örlü, and P. H. Alfredsson, Turbulent flows in curved pipes: Recent advances in experiments and simulations, Appl. Mech. Rev. **68**, 50802 (2016).
[25] J. D. Stanitz, W. M. Osborn, and J. Mizisin, *An Experimental Investigation of Secondary Flow in an Accelerating, Rectangular Elbow with 90 Degrees of Turning* (National Advisory Committee for Aeronautics, Washington, DC, 1953).
[26] W. R. Dean, Fluid motion in a curved channel, Proc. R. Soc. A **121**, 402 (1928).
[27] Y. Guo and W. H. Finlay, Wavenumber selection and irregularity of spatially developing nonlinear Dean and Görtler vortices, J. Fluid Mech. **264**, 1 (1994).

[28] P. E. Haines, J. P. Denier, and A. P. Bassom, Dean vortices in finite-aspect-ratio ducts, J. Fluid Mech. **716**, R8 (2013).

[29] J. T. Ault, K. K. Chen, and H. A. Stone, Downstream decay of fully developed Dean flow, J. Fluid Mech. **777**, 219 (2015).

[30] S. Hussen, Md. R. Islam, and R. N. Mondal, Numerical study of solution structure and nonlinear behavior of Dean flow with vortex structure in a bending square duct, Phys. Fluids **35**, 117116 (2023).

[31] C.-H. Liang, M.-B. Sun, Y. Huang, D.-P. Xiong, J. Yu, Y.-X. Yang, H.-B. Wang, Y. Sun, and G.-W. Ma, Mechanism of development of turbulent boundary layer in a curved circular pipe under supersonic conditions, AIP Adv. **12**, 35039 (2022).

[32] X. He, S. V. Apte, S. K. Karra, and Ö. N. Doğan, An LES study of secondary motion and wall shear stresses in a pipe bend, Phys. Fluids **33**, 115102 (2021).

[33] H. Chen, C. Liang, Y. Yang, M. Sun, W. Long, W. Li, H. Wang, D. Xiong, and T. Wang, Study on secondary motions in supersonic boundary layers of a bent pipe, Phys. Fluids **36**, 095166 (2024).

[34] J. A. C. Humphrey, J. H. Whitelaw, and G. Yee, Turbulent flow in a square duct with strong curvature, J. Fluid Mech. **103**, 443 (1981).

[35] K. C. Muck, P. H. Hoffmann, and P. Bradshaw, The effect of convex surface curvature on turbulent boundary layers, J. Fluid Mech. **161**, 347 (1985).

[36] R. D. Moser and P. Moin, The effects of curvature in wall-bounded turbulent flows, J. Fluid Mech. **175**, 479 (1987).

[37] P. Bradshaw, The effect of mean compression or dilatation on the turbulence structure of supersonic boundary layers, J. Fluid Mech. **63**, 449 (1974).

[38] Q. Wang and Z. Wang, An experimental investigation of the supersonic turbulent boundary layer subjected to convex curvature, Proc. Inst. Mech. Eng. Part G: J. Aerosp. Eng. **232**, 1015 (2018).

[39] M. Sun, Z. Hu, and N. D. Sandham, Recovery of a supersonic turbulent boundary layer after an expansion corner, Phys. Fluids **29**, 076103 (2017).

[40] M. R. Mokhtarzadeh-Dehghan and Y. M. Yuan, Measurements of turbulence quantities and bursting period in developing turbulent boundary layers on the concave and convex walls of a 90° square bend, Exp. Therm Fluid Sci. **27**, 59 (2002).

[41] P. Bradshaw, *Effects of Streamline Curvature on Turbulent Flow, No. AGARD-AG-169* (Advisory Group for Aerospace Research and Development, Neuilly-Sur-Seine, France, 1973).

[42] P. H. Hoffmann, K. C. Muck, and P. Bradshaw, The effect of concave surface curvature on turbulent boundary layers, J. Fluid Mech. **161**, 371 (1985).

[43] I. T. Neel, A. Leidy, R. D. Bowersox, and N. R. Tichenor, Hypersonic boundary layer with streamline curvature-driven adverse pressure gradient, in *8th AIAA Flow Control Conference* (American Institute of Aeronautics and Astronautics, Washington, DC, 2016).

[44] R. S. Barlow and J. P. Johnston, Structure of a turbulent boundary layer on a concave surface, J. Fluid Mech. **191**, 137 (1988).

[45] H. Görtler, Instabilität laminarer Grenzschichten an konkaven Wänden gegenüber gewissen dreidimensionalen Störungen, Z. Angew. Math. Mech. **21**, 250 (1941).

[46] J. Ren and S. Fu, Secondary instabilities of Görtler vortices in high-speed boundary layer flows, J. Fluid Mech. **781**, 388 (2015).

[47] D. Xu, J. Liu, and X. Wu, Görtler vortices and streaks in boundary layer subject to pressure gradient: Excitation by free stream vortical disturbances, nonlinear evolution and secondary instability, J. Fluid Mech. **900**, A15 (2020).

[48] D. Xu and X. Wu, Elevated low-frequency free-stream vortical disturbances eliminate boundary-layer separation, J. Fluid Mech. **920**, A14 (2021).

[49] W. S. Saric, Görtler vortices, Annu Rev Fluid Mech **26**, 379 (1994).

[50] N. El-Hady and A. K. Verma, Growth of goertler vorticies in compressible boundary layers along curved surfaces, in *14th Fluid and Plasma Dynamics Conference* (American Institute of Aeronautics and Astronautics, Palo Alto, CA, 1981).

[51] J. M. Floryan, On the Görtler instability of boundary layers, Prog. Aerosp. Sci. **28**, 235 (1991).

[52] A. J. Smits and J.-P. Dussauge, *Turbulent Shear Layers in Supersonic Flow*, 2nd ed. (Springer, New York, 2006).
[53] M. Grilli, S. Hickel, and N. A. Adams, Large-eddy simulation of a supersonic turbulent boundary layer over a compression–expansion ramp, Int. J. Heat Fluid Flow **42**, 79 (2013).
[54] Y. Zhuang, H. Tan, Y. Liu, Y. Zhang, and Y. Ling, High resolution visualization of Görtler-like vortices in supersonic compression ramp flow, J. Visualization **20**, 505 (2017).
[55] S. Cao, I. Klioutchnikov, and H. Olivier, Görtler vortices in hypersonic flow on compression ramps, AIAA J. **57**, 3874 (2019).
[56] P. V. Chuvakhov and V. N. Radchenko, Effect of Görtler-like vortices of various intensity on heat transfer in supersonic compression corner flows, Int. J. Heat Mass Transfer **150**, 119310 (2020).
[57] M. S. Loginov, N. A. Adams, and A. A. Zheltovodov, Large-eddy simulation of shock-wave/turbulent-boundary-layer interaction, J. Fluid Mech. **565**, 135 (2006).
[58] Y. Zhuang, H. Tan, X. Li, F. Sheng, and Y. Zhang, Letter: Görtler-like vortices in an impinging shock wave/turbulent boundary layer interaction flow, Phys. Fluids **30**, 061702 (2018).
[59] G. M. D. Currao, R. Choudhury, S. L. Gai, A. J. Neely, and D. R. Buttsworth, Hypersonic transitional shock-wave–boundary-layer interaction on a flat plate, AIAA J. **58**, 814 (2020).
[60] D. Xu, P. Ricco, and L. Duan, Görtler instability and transition in compressible flows, AIAA J. **62**, 489 (2024).
[61] L. Ciolkosz and E. Spina, An experimental study of görtler vortices in compressible flow, in *42nd AIAA/ASME/SAE/ASEE Joint Propulsion Conference & Exhibit* (American Institute of Aeronautics and Astronautics, Sacramento, CA, 2006).
[62] Q. Wang, Z. Wang, and Y. Zhao, Visualization of Görtler vortices in supersonic concave boundary layer, J. Visualization **21**, 57 (2018).
[63] L. Chen, Y. Zhang, J. Wang, H. Xue, Y. Xu, Z. Wang, and H. Tan, Görtler vortices in the shock wave/boundary-layer interaction induced by curved swept compression ramp, aerosp. **11**, 760 (2024).
[64] S. Viaro and P. Ricco, Compressible unsteady Görtler vortices subject to free-stream vortical disturbances, J. Fluid Mech. **867**, 250 (2019).
[65] M. Sun, N. D. Sandham, and Z. Hu, Turbulence structures and statistics of a supersonic turbulent boundary layer subjected to concave surface curvature, J. Fluid Mech. **865**, 60 (2019).
[66] Q. C. Wang, Z. G. Wang, M. B. Sun, R. Yang, Y. X. Zhao, and Z. Hu, The amplification of large-scale motion in a supersonic concave turbulent boundary layer and its impact on the mean and statistical properties, J. Fluid Mech. **863**, 454 (2019).
[67] D. Xiong, Y. Yang, and Y. Wang, An improved synthetic eddy method for generating inlet turbulent boundary layers, Aerospace **9**, 37 (2022).
[68] W. Long, D. Xiong, H. Wang, M. Sun, H. Chen, W. Li, and Y. Yang, Generation of inflow turbulence using an improved synthetic eddy method, Phys. Fluids **36**, 085128 (2024).
[69] N. Jarrin, S. Benhamadouche, D. Laurence, and R. Prosser, A synthetic-eddy-method for generating inflow conditions for large-eddy simulations, Int. J. Heat Fluid Flow **27**, 585 (2006).
[70] X. Wu, Inflow turbulence generation methods, Annu. Rev. Fluid Mech. **49**, 23 (2017).
[71] L. Li, H. B. Wang, G. Y. Zhao, M. B. Sun, D. P. Xiong, and T. Tang, An efficient low-dissipation hybrid central/WENO scheme for compressible flows, Int. J. Comput. Fluid Dyn. **34**, 705 (2020).
[72] G.-Y. Zhao, M.-B. Sun, and S. Pirozzoli, On shock sensors for hybrid compact/WENO schemes, Comput. Fluids **199**, 104439 (2020).
[73] J. Lai, H. Yu, Z. Tian, and H. Li, Hybrid MPI and CUDA parallelization for CFD applications on multi-GPU HPC clusters, Sci. Program. **2020**, 8862123 (2020).
[74] D. Xiong, M. Sun, J. Yu, Z. Hu, Y. Yang, H. Wang, and Z. Wang, Effects of confinement and curvature on a jet in a supersonic cross-flow, Proc. Inst. Mech. Eng. Part G: J. Aerosp. Eng. **236**, 3518 (2022).
[75] H. Chen, M. Sun, D. Xiong, Y. Yang, T. Wang, and H. Wang, Large eddy simulation of supersonic flow in ducts with complex cross-sections, Theor. Appl. Mech. Lett. **13**, 100469 (2023).
[76] T. Tang, Z. Wang, J. Yu, Y. Huang, M. Sun, H. Wang, G. Zhao, Y. Yang, and D. Xiong, Numerical study of transverse jet mixing and combustion in a high-enthalpy supersonic crossflow with trace gases, Phys. Fluids **35**, 036120 (2023).

[77] T. Tang, Z. Wang, J. Yu, Y. Huang, M. Sun, H. Wang, G. Zhao, Y. Yang, and D. Xiong, Investigation of multi-scale flow structures and combustion characteristics in a cavity-enhanced circular scramjet, Combust. Flame **264**, 113431 (2024).
[78] J. P. Monty, N. Hutchins, H. C. H. Ng, I. Marusic, and M. S. Chong, A comparison of turbulent pipe, channel and boundary layer flows, J. Fluid Mech. **632**, 431 (2009).
[79] H. Tennekes and J. L. Lumley, *A First Course in Turbulence* (MIT Press, Cambridge, MA, 1972).
[80] M. Wosnik, L. Castillo, and W. K. George, A theory for turbulent pipe and channel flows, J. Fluid Mech. **421**, 115 (2000).
[81] M. V. Morkovin, Effects of compressibility on turbulent flows, in *Mécanique de La Turbulence*, edited by A. Favre (Gordon and Breach, New York, 1962), pp. 367–380.
[82] S. Pirozzoli and M. Bernardini, Turbulence in supersonic boundary layers at moderate Reynolds number, J. Fluid Mech. **688**, 120 (2011).
[83] K. P. Griffin, L. Fu, and P. Moin, Velocity transformation for compressible wall-bounded turbulent flows with and without heat transfer, Proc. Natl Acad. Sci. USA **118**, e2111144118 (2021).
[84] E. R. Van Driest, Turbulent boundary layer in compressible fluids, J. Aeronaut. Sci. **18**, 145 (1951).
[85] P. Schlatter and R. Örlü, Assessment of direct numerical simulation data of turbulent boundary layers, J. Fluid Mech. **659**, 116 (2010).
[86] L. Duan, I. Beekman, and M. P. Martín, Direct numerical simulation of hypersonic turbulent boundary layers. Part 3. Effect of Mach number, J. Fluid Mech. **672**, 245 (2011).
[87] G. N. Coleman, J. Kim, and R. D. Moser, A numerical study of turbulent supersonic isothermal-wall channel flow, J. Fluid Mech. **305**, 159 (1995).
[88] Y. Morinishi, S. Tamano, and K. Nakabayashi, Direct numerical simulation of compressible turbulent channel flow between adiabatic and isothermal walls, J. Fluid Mech. **502**, 273 (2004).
[89] S. J. Kline, W. C. Reynolds, F. A. Schraub, and P. W. Runstadler, The structure of turbulent boundary layers, J. Fluid Mech. **30**, 741 (1967).
[90] C. R. Smith and S. P. Metzler, The characteristics of low-speed streaks in the near-wall region of a turbulent boundary layer, J. Fluid Mech. **129**, 27 (1983).
[91] J. Kim, P. Moin, and R. Moser, Turbulence statistics in fully developed channel flow at low Reynolds number, J. Fluid Mech. **177**, 133 (1987).
[92] J. Jeong and F. Hussain, On the identification of a vortex, J. Fluid Mech. **285**, 69 (1995).
[93] R. J. Adrian, Hairpin vortex organization in wall turbulence, Phys. Fluids **19**, 041301 (2007).
[94] S. Deck, Recent improvements in the zonal detached eddy simulation (ZDES) formulation, Theor. Comput. Fluid Dyn. **26**, 523 (2012).
[95] R. L. Simpson, Turbulent boundary-layer separation, Annu. Rev. Fluid Mech. **21**, 205 (1989).
[96] C. V. Krishna, N. Gundiah, and J. H. Arakeri, Separations and secondary structures due to unsteady flow in a curved pipe, J. Fluid Mech. **815**, 26 (2017).
[97] E. F. Spina, A. J. Smits, and S. K. Robinson, The physics of supersonic turbulent boundary layers, Annu. Rev. Fluid Mech. **26**, 287 (1994).
[98] L. Xue, F. F. J. Schrijer, B. W. Van Oudheusden, C. Wang, Z. Shi, and K. Cheng, Theoretical study on regular reflection of shock wave–boundary layer interactions, J. Fluid Mech. **899**, A30 (2020).
[99] N. T. Clemens and V. Narayanaswamy, Low-frequency unsteadiness of shock wave/turbulent boundary layer interactions, Annu. Rev. Fluid Mech. **46**, 469 (2014).
[100] H. H. Fernholz and P. J. Finley, *A Critical Commentary on Mean Flow Data for Two-Dimensional Compressible Turbulent Boundary Layers* (Advisory Group for Aerospace Research and Development, Neuilly-Sur-Seine, France, 1980).
[101] H. Görtler, *On the Three-Dimensional Instability of Laminar Boundary Layers on Concave Walls*, Report No. NACA-TM-1375, NASA NTRS (National Advisory Commitee for Aeronautics, Washington, DC, 1954).
[102] Z. Zhang, J. Hao, and K. C. K. Uy, Characterising Görtler vortices in supersonic turbulent flows over concave surfaces, J. Fluid Mech. **1012**, A29 (2025).
[103] J. Z. Wu, H. Y. Ma, and M.-D. Zhou, *Vorticity and Vortex Dynamics* (Springer, Berlin, 2006).
[104] S. B. Pope, *Turbulent Flows*, 1st ed. (Cambridge University Press, Cambridge, 2000).

[105] S. S. Lu and W. W. Willmarth, Measurements of the structure of the Reynolds stress in a turbulent boundary layer, J. Fluid Mech. **60**, 481 (1973).
[106] D. Pokrajac, L. J. Campbell, V. Nikora, C. Manes, and I. McEwan, Quadrant analysis of persistent spatial velocity perturbations over square-bar roughness, Exp. Fluids **42**, 413 (2007).
[107] N. R. Tichenor, R. A. Humble, and R. D. W. Bowersox, Response of a hypersonic turbulent boundary layer to favourable pressure gradients, J. Fluid Mech. **722**, 187 (2013).